Published online 15 February 2016

Nucleic Acids Research, 2016, Vol. 44, No. 7 ***3373–3389***
doi: 10.1093/nar/gkw073

Mapping of internal monophosphate 5′ ends of *Bacillus subtilis* messenger RNAs and ribosomal RNAs in wild-type and ribonuclease-mutant strains

Jeanne M. DiChiara[1], Bo Liu[1], Sabine Figaro[2], Ciarán Condon[2] and David H. Bechhofer[1,*]

[1]Department of Pharmacology and Systems Therapeutics, Icahn School of Medicine at Mount Sinai, Box 1603, 1 Gustave L. Levy Place, New York, NY 10029, USA and [2]CNRS UMR8261 (affiliated with Université Paris Diderot, Sorbonne Paris Cité), Institut de Biologie Physico-Chimique, 13 rue Pierre et Marie Curie, 75005 Paris, France

Received April 24, 2015; Revised January 27, 2016; Accepted January 29, 2016

ABSTRACT

The recent findings that the narrow-specificity endoribonuclease RNase III and the 5′ exonuclease RNase J1 are not essential in the Gram-positive model organism, *Bacillus subtilis*, facilitated a global analysis of internal 5′ ends that are generated or acted upon by these enzymes. An RNA-Seq protocol known as PARE (Parallel Analysis of RNA Ends) was used to capture 5′ monophosphorylated RNA ends in ribonuclease wild-type and mutant strains. Comparison of PARE peaks in strains with RNase III present or absent showed that, in addition to its well-known role in ribosomal (rRNA) processing, many coding sequences and intergenic regions appeared to be direct targets of RNase III. These target sites were, in most cases, not associated with a known antisense RNA. The PARE analysis also revealed an accumulation of 3′-proximal peaks that correlated with the absence of RNase J1, confirming the importance of RNase J1 in degrading RNA fragments that contain the transcription terminator structure. A significant result from the PARE analysis was the discovery of an endonuclease cleavage just 2 nts downstream of the 16S rRNA 3′ end. This latter observation begins to answer, at least for *B. subtilis*, a long-standing question on the exonucleolytic versus endonucleolytic nature of 16S rRNA maturation.

INTRODUCTION

Regulation of bacterial gene expression occurs by transcriptional and translational control, as well as by regulating mRNA decay and processing, which modulates the amount and suitability of an mRNA available for translation. In *Bacillus subtilis*, mRNA processing generally occurs by a number of relatively non-specific enzymes: the endonuclease RNase Y, the 5′-to-3′ exonuclease RNase J1, several 3′-to-5′ exoribonucleases and one or more RNA pyrophosphohydrolases (RppH) (1–7). Decay is initiated either by (1) RppH-mediated conversion of the 5′-terminal triphosphate to a monophosphate, giving RNase J1 access to degrade in the 5′-to-3′ direction, or (2) RNase Y internal cleavage(s), which generates a downstream fragment that is degraded by RNase J1 and an upstream fragment that is degraded by 3′ exonucleases. None of the genes encoding individual RNases or pyrophosphohydrolases are essential, including the genes for RNase J1 and RNase Y, as we have shown (8). The activities of these enzymes on specific mRNAs can be controlled by 5′-proximal RNA structure (9), 5′-terminal nucleotide sequence (10), ribosome flow (11) and RNA-binding proteins (12).

In contrast to the relatively non-specific nature of the ribonucleases mentioned above, *B. subtilis* RNase III, encoded by the *rnc* gene, is a narrow-specificity enzyme that recognizes particular double-stranded RNA (dsRNA) structures (13,14). Virtually all bacterial species appear to contain at least one RNase III-like protein, which is characterized by a specific endonuclease domain (the RNase III domain) and a dsRNA-binding domain. RNase III can cleave one strand or both strands of a double-stranded target (13). Long-known native targets of *B. subtilis* RNase III are precursor 30S ribosomal RNA (rRNA) (15) and small cytoplasmic RNA (scRNA) encoded by the *scr* gene (16). In the case of rRNA, dsRNA stems on either side of 16S and 23S precursor rRNA are cleaved by RNase III. Further 5′-end maturation of 16S rRNA occurs by an unknown endonuclease cleavage, followed by RNase J1 exonucleolytic processing to the mature 5′ end (17). The nature of 16S rRNA 3′-end maturation has not been elucidated. *B. subtilis* also contains a second RNase III-like protein named Mini-III, which consists of only the RNase III catalytic domain and which catalyzes 23S rRNA maturation directly (18). We and others have also characterized non-native targets of RNase III encoded by phage SP82 (19,20).

*To whom correspondence should be addressed. Tel: +1 212 241 5628; Fax: +1 212 996 7214; Email: david.bechhofer@mssm.edu

Bacillus subtilis RNase III was thought to be essential, as the *rnc* gene encoding the enzyme could not readily be deleted (15). Condon *et al*. (3) used a tiling microarray to study the effect of a 30-fold reduction in RNase III concentration in *B. subtilis*, and found a significant (≥2-fold) effect on 11% of coding sequences (CDSs). Most of the changes in gene expression were due to transcriptional effects rather than direct cleavage by RNase III. The current study on the effect of *B. subtilis* RNase III was initiated after a more recent study showed that, in fact, RNase III is not essential in *B. subtilis* (21). Rather, the inability to delete *rnc* is due to expression of toxin genes carried on the Skin and SPβ prophages. mRNAs encoded by these genes are targeted for cleavage by RNase III when they complex with complementary non-coding RNAs. In the absence of RNase III, the toxin mRNAs accumulate, resulting in lethal levels of toxin proteins. In a strain deleted for the Skin and SPβ prophages, RNase III is no longer essential and the strain grows normally (21).

In other organisms, there are several well-known examples of gene regulation by RNase III cleavage of mRNA, including, in *Escherichia coli*, autoregulation of the *rnc* gene (22–24) and regulation of the *rpsO-pnp* operon (25,26). In these cases, RNase III cleavage in a leader region results in destabilization of the mRNAs. Kushner *et al*. used tiling microarrays to examine gene expression in an *E. coli* RNase III null mutant. They found significant (1.5-fold) decreased or increased expression of 12% of CDSs (27), many of which were due to indirect effects (e.g., transcriptional). These authors reported the first known instance of a CDS (*nirB*) directly targeted by RNase III. More recently, Schroeder *et al*. used a dsRNA-specific antibody to probe for dsRNAs in *E. coli* wild-type and *rnc* mutant strains, and found abundant sense/antisense pairings that were RNase III targets (28). Additional evidence of CDS cleavage by RNase III was obtained in studies of RNase III targets in *Staphylococcus aureus* (24) and *Streptomyces coelicolor* (29). These studies used immunoprecipitation of RNA fragments bound to an inactive RNase III enzyme to identify RNase III targets. Large numbers of antisense RNAs were identified as RNase III substrates in the former study (24). Pervasive processing of sense–antisense pairings by RNase III has been suggested by other experiments in *S. aureus*, with evidence that the same occurs in *B. subtilis* (30).

In the current study, we adapted to *B. subtilis* an RNA-Seq-based method of mapping 5′-monophosphorylated ends, first used in *Arabidopsis* experiments (31–33). The method was able to directly identify RNase III cleavage sites on a global scale, to discover an endonuclease cleavage that is involved in 3′ end maturation of 16S rRNA, and to demonstrate the importance of RNase J1 on 3′-terminal fragment turnover.

MATERIALS AND METHODS

Strains and growth conditions

Bacterial strains used in this study are listed in Table 1. For RNA isolation, cells were grown overnight in Luria Broth (LB medium) plus antibiotic at 37°C, and then diluted 1:50 for growth until mid-log phase (Klett ∼70) without antibiotic. Concentrations of antibiotics were: chloramphenicol 4 μg/ml, erythromycin 5 μg/ml, kanamycin 5 μg/ml, phleomycin 2 μg/ml, spectinomycin 200 μg/ml. For analysis of *putP* mRNA, strains were grown in a modified Spizizen minimal medium supplemented with proline: 1.4% K_2HPO_4, 0.6% KH_2PO_4, 0.1% Na citrate•$2H_2O$, 1 mM $MgSO_4$•$7H_20$, 0.5% glucose, 60 μg/ml threonine, 60 μg/ml tryptophan, 0.01% proline.

The strain carrying the *rnc* E138A mutation was made as follows: the wild-type *rnc* CDS carried on plasmid pBSR2 (34) was disrupted with a chloramphenicol (Cm)-resistance gene, giving plasmid pJMD2. Strain BG875, the W168 derivative with Skin and SPβ phage deletions, was transformed to Cm resistance with ScaI-linearized plasmid pJMD2 to give strain BG908. The *rnc* CDS carried on plasmid pJMD1, a derivative of pYH250 (35), was mutagenized with the QuikChange protocol (Agilent Technologies), to give the E138A mutation on plasmid pJMD3. (The sequences of oligonucleotides used in this study are given in Table S1.) BG908 was transformed with ApaI-linearized pJMD3 and plasmid pMAP65 (36), to select for phleomycin-resistant cells that were transformed by plasmid pMAP65 and possibly co-transformed with pJMD3. Approximately 2000 colonies were screened for loss of Cm resistance and one colony was obtained that carried the *rnc* E138A substitution for wild-type *rnc*. This strain was designated BG917. BG917 was cured of pMAP65 by growing cells without phleomycin selection in the presence of 0.006% sodium dodecyl sulphate (SDS) (37). After several passages into fresh media, strain BG923 was obtained.

The strains for the drop collapse assay were constructed by transforming BG935 chromosomal DNA into BG875 and BG923 to yield BG940 and BG942, respectively. Similarly, strains BG983 and BG984 were constructed by transforming BG875 and BG877, respectively, with BG981 chromosomal DNA. Gene knockouts were confirmed by polymerase chain reaction (PCR), and mutations were confirmed by sequencing.

Growth curves

After overnight growth in 2X YT medium, duplicate samples of cells were diluted 1:20 in water and the OD_{600} was adjusted to 0.2. A 96-well plate was prepared with 190 μl of 2× YT medium to which 10 μl of each sample was added. Cells were grown in a BioTek PowerWave XS2 Microplate Spectrophotometer with shaking for 24 h at 37°C, with kinetic reads taken at 1 h intervals. To calculate doubling time, the kinetic readings were plotted on a semi-log graph in Microsoft Excel. The linear regression function was then used to determine the doubling time for the linear (logarithmic growth) portion of the curve, using the equation doubling time = $\log_2$/slope.

RNA isolation and Northern blotting

RNA was isolated using the hot phenol method, as described (38). RNA concentrations were measured using a Qubit 2.0 Fluorometer (Invitrogen) and concentrations were adjusted to give equal amounts of RNA loaded per lane. Before Northern blot analyses, RNA samples were run on a MOPS gels to check RNA quality and quantity by comparing rRNA band intensities.

Table 1. Strains used in this study

Strain	Genotype	Designation in this study	Source or reference
BG578	W168 Pspac-*rnjA* ery pMAP65 kan		(65)
BG875	W168 ΔSkin ΔSPβ::PIID-*sspB* kan	*rnc*$^+$ (*rnc*$^+$ sfp$^-$ in Figure 4C)	(21) 'CCB364'
BG876	W168 ΔSkin ΔSPβ::PIID-*sspB* kan Δ*rnc::spc*		(21) 'CCB422'
BG877	W168 ΔSkin ΔSPβ::PIID-*sspB* kan Δ*rnc::ery*	Δ*rnc*	(42)
BG879	W168 ΔSkin ΔSPβ::PIID-*sspB* kan Δ*rnc::ery* Δ*rnjA::spc*	Δ*rnc* Δ*rnjA*	(42)
BG880	W168 ΔSkin ΔSPβ::PIID-*sspB* kan Δ*rnjA::spc*	*rnc*$^+$ Δ*rnjA*	(42,68)
BG898	W168 Pspac-*rnjA* ery Δ*rny::spc* pMAP65 kan		This study
BG908	W168 ΔSkin ΔSPβ::PIID-*sspB* kan Δ*rnc::cat*		This study
BG917	W168 ΔSkin ΔSPβ::PIID-*sspB* kan *rncE138A* (pMAP65)		This study
BG923	W168 ΔSkin ΔSPβ::PIID-*sspB* kan *rncE138A*	*E138A*	This study
BG935	W168 *sfp*$^+$ *Em*		R. Kolter laboratory
BG940	W168 ΔSkin ΔSPβ::PIID-*sspB* kan *sfp*$^+$ *Em*	*rnc*$^+$ sfp$^+$ in Figure 4C	This study
BG942	W168 ΔSkin ΔSPβ::PIID-*sspB* kan *sfp*$^+$ *Em rncE138A*	*rnc*$^-$ sfp$^+$ in Figure 4C	This study
BG981	SMY Δ*putR::cat*		(45) 'BB3330'
BG983	W168 ΔSkin ΔSPβ::PIID-*sspB* kan Δ*putR::cat*	*rnc*$^+$ Δ*putR*	This study
BG984	W168 ΔSkin ΔSPβ::PIID-*sspB* kan Δ*rnc::ery* Δ*putR::cat*	Δ*rnc* Δ*putR*	This study
BG994	W168 ΔSkin ΔSPβ::PIID-*sspB* kan *amyE*::P_{spac}-*putP*		This study
BG995	W168 ΔSkin ΔSPβ::PIID-*sspB* kan *amyE*::P_{spac}-*putP* Δ*rnc::ery*		This study
CCB434	W168 Δ*rnjA::spc*		(8)
CCB441	W168 Δ*rny::spc*		(8)
CCB418	W168 *txpA-10Δ* Δ*yonT::ery* Δ*rnc::spc*		(3)
CCB078	W168 Δ*rnjB::spc*		(65)
CCB501	W168 Δ*rnjB::spc* Δ*rnjA::kan* (W168 version of CCB449)		(8)

Total RNA was separated on denaturing polyacrylamide gels (6% polyacrylamide/7M urea) or denaturing agarose gels (1.5% agarose/7% formaldehyde MOPS) and blotted onto positively-charged nylon membranes (Amersham HyBond N$^+$; GE Healthcare). Hybridizations were performed in roller bottles with varying conditions depending on whether a 5′ end-labeled oligonucleotide or riboprobe was used. Band signal intensity from each lane was normalized by stripping blots and probing for 16S rRNA, using an oligonucleotide complementary to 1405–1424 nts (39).

Parallel analysis of RNA ends (PARE)

The PARE protocol described previously (32) was adapted to *B. subtilis* (see Supplementary Figure S1). Ribosomal RNA was removed from 5 μg of total RNA using the Ribo-Zero^{TM} rRNA Removal Kit for Gram-Positive Bacteria (Illumina), per the manufacturer's protocol. RNA concentrations in rRNA-depleted samples were determined with a Qubit 2.0 Fluorometer (Invitrogen). Equal amounts of samples were used to construct the PARE libraries using the NEBNext Multiplex Small RNA Library Prep Set for Illumina (Set 1). The manufacturer's protocol was modified so that 5′ monophosphorylated ends that result from endonuclease cleavage or pyrophosphohydrolase activity were preferentially selected. Briefly, after 3′ SR Adaptor ligation, reverse transcriptase (RT) primer hybridization and 5′ SR Adaptor ligation — performed as per the manufacturer's protocol — the reaction mixture volume was brought to 100 μl and samples were cleaned up with the RNeasy MinElute Cleanup Kit (Qiagen). A total of 12 μl of RNA was recovered following the manufacturer's protocol. The RNA was fragmented using the NEBNext® Magnesium RNA Fragmentation Module at 94°C for 4 min, and 2 μl of stop solution was added. After a second RNeasy MinElute cleanup, half of the RNA (6 μl) was again ligated to the 3′ SR Adaptor. Thus, after magnesium fragmentation only RNAs that retained their 5′ SR Adaptor (and original 5′ monophosphate) would undergo subsequent RT and PCR amplification. After addition of the RT primer, the reaction volume was adjusted to 30 μl and RT/PCR amplification reactions were performed as per the manufacturer's protocol, using barcoded primers.

One-tenth of the PCR reaction was run on a 1.5% agarose gel to visualize the library, which consisted of cDNA ranging from 50 to ∼500 nts. A total of 20 μl of the cDNA library were prepared for Illumina sequencing using a 1.5× volume of Agencourt AMPure XP Beads (Beckman Coulter), according to the manufacturer's instructions. The procedure was repeated twice, and the sample was eluted in a final volume of 20 μl. Samples were stored at −80°C. Prior to sequencing, each sample was checked on an Agilent BioAnalyzer. Samples that contained >125 bp cDNA were used for 50-nts single-end RNA-Seq reads on an Illumina MiSeq slide. Reads were mapped to the *B. subtilis* genome as described (5).

5′ RLM-RACE

Total RNA (250 ng) was used for each sample. The 5′ SR Adaptor from the NEBNext Multiplex Small RNA Library Prep Set for Illumina (Set 1) was ligated to RNA at 25°C for 1 h. Primer extension was performed as described previously (40), using the SuperScript III protocol from Invitrogen. PCR amplification was performed using *Taq* PCR Master Mix Kit (Qiagen) and the following conditions: 94°C/3 min, 30 cycles of 94°C/30 s, 55°C/30 s, 72°C/30 s and 5 min extension at 72°C. Nested PCR was then performed on 1 μl of the primary PCR reaction as template, using the same conditions as above. Primer sequences are given in Supplementary Table S1.

A total of 10 μl of the final PCR reaction was visualized on a native 6% polyacrylamide gel. The remainder of samples that displayed bands in the *rnc*$^+$ strain only was run on

a preparative 6% native polyacrylamide gel. The band of interest was cut out and soaked overnight at 37°C in 300 μl of RNA diffusion buffer (0.5 M ammonium acetate, 2 mM ethylenediaminetetraacetic acid, 0.2% SDS). The eluate was extracted with phenol:chloroform (1:1) and ethanol precipitated. The precipitate was resuspended in 10 μl of water and ligated into the PCR cloning vector, pGEM-T (Promega), for cloning and sequencing.

Drop-collapse assay

For the qualitative assay, cultures were grown overnight in 5 ml LB with erythromycin at 5 μg/ml. A total of 100 μl of the overnight culture was pelleted and 5 μl of supernatant was carefully added to 5 μl of water that was placed on the lid of a square petri dish. The drops were allowed to sit for several minutes before being photographed. The amount of spreading of the water droplet corresponded to the amount of surfactin in the culture supernatant.

For the quantitative assay, purified surfactin (Sigma #S3523) was dissolved in 1 ml 100% ethanol for a 10 mg/ml stock solution, which was diluted 1:100 in LB media to give a 100 μg/ml working solution of surfactin. Overnight cultures grown in 5 ml LB + erythromycin were pelleted and dilutions of the supernatant were prepared. The drop collapse assay was performed as above, using control surfactin dilutions (100, 50, 25, 12.5 and 6.25 μg/ml) and culture supernatant dilutions (undiluted, 1:2, 1:4, 1:8, 1:16, 1:32). The amount of surfactin present in each supernatant was calculated comparing the highest dilution of supernatant where drop collapse was observed to the control surfactin dilutions.

RESULTS

RNase III-generated 5′ ends

Experiments to map RNase III 5′ ends were performed in strains that were: deleted for the Skin and SPβ prophages to render *rnc* non-essential; deleted for the *rnjA* gene encoding the 5′ exonuclease RNase J1; and either *rnc* wild-type (*rnc*$^+$) or *rnc* deleted (Δ*rnc)* (see Table 1 for strains used in this study). We used strains that were deleted for *rnjA* in the expectation that this would better preserve 5′ ends that were generated by RNase III. Growth rates were determined for *rnc*$^+$ and Δ*rnc* strains, with or without *rnjA* present (Table 2). While the absence of RNase J1 caused a major slowing of the growth rate, proportionally similar to what was observed previously (8), this was not affected by the presence or absence of RNase III. Apparently, alternate pathways for rRNA processing are sufficient to allow normal growth, and the lack of processing of many other mRNAs that are RNase III targets (see below) does not result in an effect on growth rate in rich medium.

5′ ends generated by RNase III were mapped by the PARE method (31). Total RNA was isolated from exponential phase cultures of *rnc*$^+$ and Δ*rnc* strains grown in LB medium. After rRNA depletion, the RNA preparation was processed by the PARE protocol (Supplementary Figure S1; see 'Materials and Methods' section). Briefly, RNA molecules used to prepare the PARE library would have either a 5′-triphosphate end representing a transcription start site (TSS) or a 5′-monophosphate end. The latter could be generated by RppH activity at the TSS, or by endonucleolytic cleavage internally. Ligation of adapters to 5′-monophosphorylated and 3′ hydroxylated ends, followed by amplification, created a PARE library that was subject to 50-nts reads, starting at the junction of the 5′ adaptor with the 5′ end of the RNA fragment. The chromosomal location of a 5′ monophosphorylated end was identified as the first position in a ∼50-nts read. As discussed below, the PARE method does not always identify the exact 5′ end of an RNA. The term 'PARE peak' was used to refer to a stretch of increased reads that begins with a 5′ monophosphate end putatively generated by *in vivo* processing.

Table 2. Growth rate of *rnc*$^+$ and Δ*rnc* strains

Strain	Doubling time
rnc$^+$	43.4
Δ*rnc*	43.1
rnc$^+$ Δ*rnjA*	145.7
Δ*rnc* Δ*rnjA*	153.8

PARE protocol validation—scRNA

Previous work had identified major and minor RNase III cleavage sites in scRNA (16,41), which are indicated in Figure 1A (cleavage sites IIIA and IIIb). The mature 5′ end of scRNA is generated directly by RNase III cleavage at 38 nts, while the mature 3′ end is primarily the result of RNase Y cleavage at around 320 nts, followed by exonucleolytic trimming to 308 nts (42). In the current analysis, the PARE read data from the *rnc*$^+$ strain showed a prominent 5′-proximal PARE peak beginning at scRNA 38 nts (Figure 1B, top panel), the nucleotide at which the major RNase III cleavage site had been mapped previously. (There is a minor shoulder of a few nucleotides preceding the major peak at 38 nts. This is observed frequently in the PARE data, and may reflect additional cleavages by other endonucleases in the region of a major RNase III cleavage site.) This result indicated that the PARE protocol could reliably identify RNase III cleavage sites *in vivo*.

There was no PARE peak for the scRNA minor 3′-proximal RNase III cleavage at 313 nts (Figure 1B, top panel), which was not unexpected, as the major 3′-proximal cleavage is catalyzed by RNase Y at 321 nts (42), for which a PARE peak is observed (Figure 1B, top panel). This peak is not as prominent as that of the scRNA 5′ end, likely because the fragment generated by this peak is turned over, whereas the mature scRNA containing the 5′ end at 38 nts is stable. The RNase Y PARE peak is obscured in a strain that is deleted for RNase Y (Figure 1B, bottom panel). Instead, a strong PARE peak beginning at the secondary RNase III cleavage site is detected, as has been observed by Northern blot analysis (42).

In the Δ*rnc* deletion strain, the 5′-proximal PARE peak was shifted upstream by 6 nts (Figure 1B, middle panel). We have previously examined this cleavage by Northern blot and primer extension analyses, and confirmed that the 5′ end is several nucleotides upstream of the mature 5′ end in the *rnc*$^+$ strain (42). We suggested that this cleavage, by

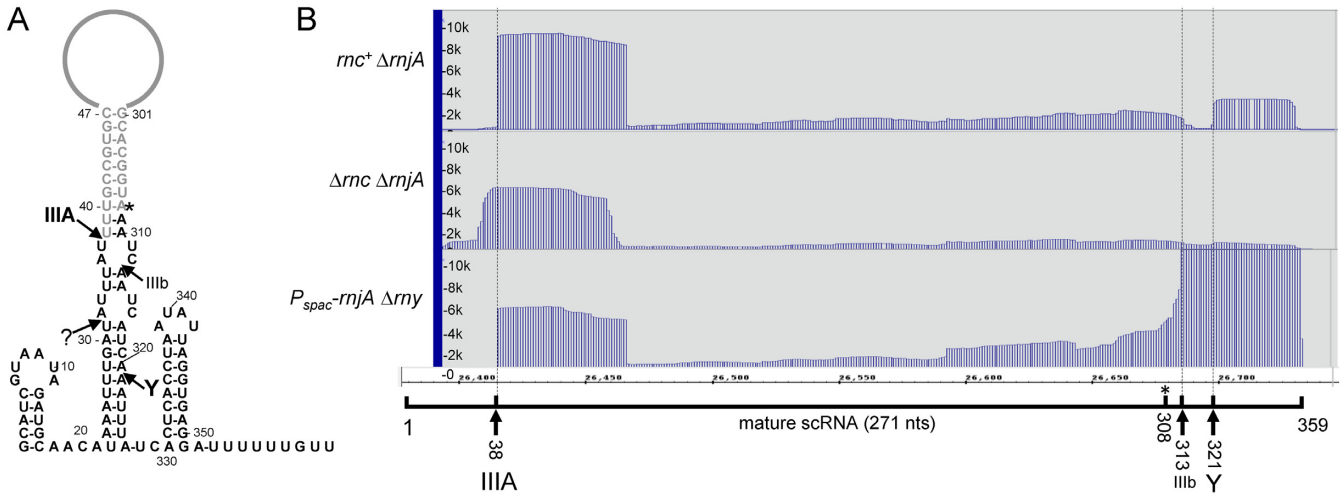

Figure 1. Analysis of scRNA. (**A**) Schematic diagram of scRNA, showing major sites of RNase III (IIIA) and RNase Y (Y) cleavage. Minor site of RNase III cleavage (IIIb) is also indicated. Sequences present in the fully-processed scRNA are shown in gray. The mature 5′ end is created directly by RNase III cleavage at 38 nts, and the mature 3′ end is created by RNase Y cleavage, followed by 3′ exonuclease trimming to 308 nts (asterisk). (**B**) PARE data for scRNA in three strains, with genotypes indicated at left. Below the PARE data is a schematic of the 359-nts scRNA transcript with endonuclease cleavage sites indicated and correlated with PARE peaks.

an unknown endonuclease, may represent a quality control mechanism to initiate degradation of scRNA that is not processed by RNase III.

Messenger RNA targets of RNase III

PARE data were analyzed for peaks that mapped to mRNA sites and that were significantly more prominent in the *rnc*$^+$ strain than the Δ*rnc* strain. To account for changes in gene expression caused indirectly by the loss of RNase III (e.g., transcriptional effects), RNA samples from the *rnc*$^+$ and Δ*rnc* strains were also subject to a standard RNA-Seq analysis (Supplementary Table S2). For CDSs that had a read coverage of at least 1.0 read per base in both strains (2414 genes), the absence of RNase III resulted in a >2-fold increase in 209 genes and a >2-fold decrease in 329 genes. This amounts to significant effects on ∼13% of the *B. subtilis* genome, which is similar to the effect of an RNase III depletion found previously (3), although the strains that were used in the previous study were *rnjA* wild-type. For PARE peaks with an average of >100 reads per position in the peak, we calculated the ratio of PARE reads in *rnc*$^+$ and Δ*rnc* strains, and divided this by the ratio of RNA-Seq reads over the same positions in *rnc*$^+$ and Δ*rnc* strains, to give a 'ratio of ratios' or 'RR.' Sites with a high RR value are those that are highly likely to be direct targets of RNase III cleavage, rather than due to indirect effects of the presence or absence of RNase III on gene expression. After normalizing PARE reads, we tallied 53 mRNAs and 5 intergenic RNAs that had one or more peaks with an RR of >10 (Table 3), a conservatively high threshold. Of the 53 mRNA targets, there was no bias toward any gene functional category (data not shown), nor was there bias to the operonic position of the CDS (Table 3). For only four of these genes were cleavage sites mapped to genomic positions that have identified antisense RNA transcripts, according to recent transcriptome mapping data (43) (Table 3).

Predicted structure of selected RNase III target sites

As mentioned, in many cases the start of a PARE peak was preceded by a shoulder representing a low level of 5′ ends upstream of an actual RNase III cleavage site. These may be due to cleavage by another activity (e.g., RNase Y) in a neighboring upstream region. We therefore used 5′ RNA ligation-mediated rapid amplification of cDNA ends (5′ RLM-RACE) to map more precisely 5′ ends in mRNA regions that were predicted by PARE to be RNase III target sites. Thirteen genes were selected for 5′ RLM-RACE experiments, and six genes for which the RLM-RACE protocol gave a clear PCR product of the predicted size in the *rnc*$^+$ strain and no comparable product in the Δ*rnc* strain were analyzed (cf. Figure 2A and Supplementary Figure S2). The 5′ ends mapped by RLM-RACE were, in most cases, either at the site mapped by PARE or a few nucleotides away (Table 4; see 'Discussion' section).

The predicted secondary structures surrounding confirmed RNase III cleavage sites, according to mfold (44), are shown in Figure 2. Several of these—*putP*, intergenic *cysC-sumT*, *priA* (Figure 2B–D)—show classic RNase III target sites with cleavage on one or both sides of a relatively stable, stem-loop structure with small internal bulges (13,14). For *putP*, 5′ RLM-RACE mapping gave only cleavages on the downstream side, but the PARE data and follow-up Northern blot analysis (see below) indicated an additional cleavage on the upstream side of the stem-loop, as shown by the open arrow in Figure 2B. Cleavage of *srfAA* mRNA occurred in a similar stem-loop structure, but the actual cleavage site was in a predicted loop portion and the predicted stability of the overall structure was weak (Figure 2E). The *fpiA* cleavage site was also in a loop segment, and the predicted secondary structure for this region included a relatively large internal loop region (Figure 2F). Finally, the *rnc* gene itself was found to have an RNase III cleavage site (see

Table 3. Genes with RR value > 10

	Position	Peak start	Avg depth	*rnc*$^+$ Δ*rnjA* reads	Δ*rnc* Δ*rnjA* reads	Peak RR	Operon position	Antisense overlap
1	BSU00090,guaB	16 250	112.37	409.31	126.56	11.3	monocistronic	
2	BSU00400,yabE	49 142	219.45	23.04	12.26	16.5	monocistronic	S25
3	5′_BSU00490,spoVG	55 847	112.38	157.86	25.73	11.1	monocistronic	
4	BSU01060,ybxB	121 313	142.38	2.17	3.28	39.5		
5	BSU01260,rplN	140 709	134.50	88.14	197.09	10.1		
6	5′_BSU02040,ybdN	224 045	505.79	0.90	1.43	14.4		
7	BSU03220,ycgO (putP)	348 421	148.67	8.61	1.24	63.6	3	S117
8	BSU03480,srfAA	377 519	123.54	20.75	26.72	36.7	1	
9	BSU03670,dtpT	417 038	186.39	17.46	75.24	14.1	monocistronic	
10	BSU03830,yclQ	435 313	116.07	25.41	18.56	67.1	4	
11	3′_BSU07560,pel	829 226	221.39	3.52	10.28	11.1	monocistronic	
12	BSU09640,yhdY	1 039 831	362.95	3.09	8.79	12.0		
13	BSU11590,yjbL	1 236 790	114.19	2.67	2.99	20.0		
14	BSU12100,yjeA	1 281 630	218.17	6.47	23.37	12.3	monocistronic	
15	BSU13490,ykrL (htpX)	1 415 027	384.04	21.01	46.98	11.1		
16	5′_BSU14629,ykzW	1 534 091	131.12	1.35	7.71	13.9		
17	BSU14629,ykzW<>BSU14630,speA	1 534 171	1553.17			11.0		
18a	BSU15140,mraW	1 581 006	325.37	240.06	27.30	17.3	2	
18b	BSU15140,mraW	1 581 170	996.75			17.8		
19	BSU15210,spoVE	1 590 701	272.95	32.89	56.27	13.4	4	
20	BSU15600,cysC<>BSU15610,sumT	1 633 979	203.72			151.9	4, 5	
21	BSU15710,priA	1 645 900	124.22	6.20	3.07	150.4		
22	BSU15910,fabG	1 664 924	113.09	22.84	27.53	14.0	4	
23	BSU16550,dxr	1 723 065	459.63	9.55	14.64	10.8		
24	BSU17450,glnR	1 878 240	754.45	21.72	36.29	17.5	1	
25	BSU17460,glnA	1 878 611	125.00	82.86	130.06	12.1	2	
26	BSU18080,yneT	1 932 721	148.30	4.03	14.47	19.0		
27a	BSU18380,iseA	2 002 730	165.90	27.50	31.30	81.9	monocistronic	
27b	BSU18380,iseA	2 002 958	118.29			26.9		
27c	3′_BSU18380,iseA	2 003 024	462.58			12.6		
28	BSU19650,yodM	2 137 281	144.57	0.93	1.45	35.5		
29	BSU22370,aspB	2 348 163	180.94	39.47	35.00	10.6		
30	BSU22840,engA	2 391 372	183.00	7.43	17.65	14.9		
31	BSU23860,yqjI (gndA)	2 481 775	315.90	95.85	93.23	13.3	2	
32	BSU24620,tasA	2 553 194	120.35	7.07	25.36	23.2	3	
33	BSU24930,yqzD	2 576 623	177.29	9.89	13.42	21.8	1	
34	5′_BSU24990,pstS	2 580 671	1311.06	1.39	2.36	24.9	1	
35	BSU25380,yqfA (floA)	2 618 398	130.36	21.74	18.18	10.8	2	
36a	BSU25440,yqeU (rsmE)	2 623 390	129.62	56.28	40.18	14.9	8	
36b	BSU25440,yqeU (rsmE)	2 623 510	248.82			50.8		
36c	BSU25440,yqeU (rsmE)	2 623 742	150.14			16.9		
37	5′_BSU26619,yrzO	2 720 474	195.94	0.28	0.41	31.7		
38	BSU32060,yuiD	3 298 413	116.50	9.05	6.48	12.1	monocistronic	
39	5′_BSU32070,yuiC	3 298 554	347.87	1.52	1.31	10.6	monocistronic	
40	BSU32110,yumC	3 302 457	181.23	28.59	24.35	10.7	monocistronic	
41	BSU32200,yutJ	3 309 256	136.70	16.88	44.65	11.7	monocistronic	
42	5′_BSU33000,htrB	3 385 425	369.02	7.84	12.42	14.8	monocistronic	
43	BSU33950,cggR	3 483 532	158.65	3.88	15.76	13.4	1	
44	BSU34780,yvcI<>BSU34790,trxB	3 573 049	2938.41			10.2		
45	BSU35650,lytR (tagU)	3 663 332	241.83	8.00	15.44	11.3	monocistronic	
46a	BSU36410,mbl	3 747 544	169.82	26.15	45.07	13.0	3	
46b	BSU36410,mbl	3 748 034	219.33			19.6		
47	5′_BSU36510,amtB	3 756 769	129.14	4.92	19.76	26.8	1	
48	3′_BSU36520,glnK	3 758 290	877.27	7.79	24.15	12.9	2	
49	BSU36760,murAA	3 778 464	134.98	59.60	233.24	10.6	monocistronic	S1420
50	BSU36830,atpA	3 784 404	108.89	65.91	132.29	16.3	6	
51	BSU37150,pyrG	3 811 842	144.96	14.23	55.65	10.7	monocistronic	
52	BSU37330,argS	3 833 842	174.20	68.10	60.87	19.6	monocistronic	
53	BSU37800,yweA<>BSU37810,spsL	3 882 701	199.16			13.9		
54	BSU38680,yxlD	3 969 858	131.02	0.95	1.12	14.4	3	
55	BSU39250,yxiE	4 031 849	190.50	55.90	19.72	10.5	3	
56	BSU39270,bglP<>BSU39280,yxxE	4 031 756	35479.18			15.9	1	
57	BSU39400,pdp	4 049 094	120.11	34.94	63.68	23.0	4	
58	BSU41030,jag	4 213 719	137.46	35.23	76.43	10.8	2	S1579

below), and this region showed a stable but complex predicted secondary structure (Figure 2G).

putP mRNA

We investigated further several mRNAs that were newly-identified targets of RNase III. The *putP* gene encodes a proline transporter and is part of a three-gene operon, *putBCP*, involved in proline uptake and utilization (Figure 3A). The *putBCP* operon is transcribed from a promoter that is negatively regulated by CodY in the absence of external proline (45), and positively regulated by PutR in the presence of elevated levels of external proline (45–47). The *putP* gene is also transcribed from a constitutive promoter that is located in the adjacent *putC* gene, 140-bp upstream of the *putC* stop codon (Figure 3A) (45,47). PARE and RLM-RACE data indicated an RNase III cleavage at ∼150-nts upstream from the *putP* stop codon, with a high RR value of 63.6 (Figure 3B; Table 3). Note that, in both strains, there is a PARE peak near the 3′ end of the *putP* CDS, which begins about 15-nts upstream of the strong *putP* transcription terminator structure ($\Delta G_0 = -26.6$ kcal/mol). We found

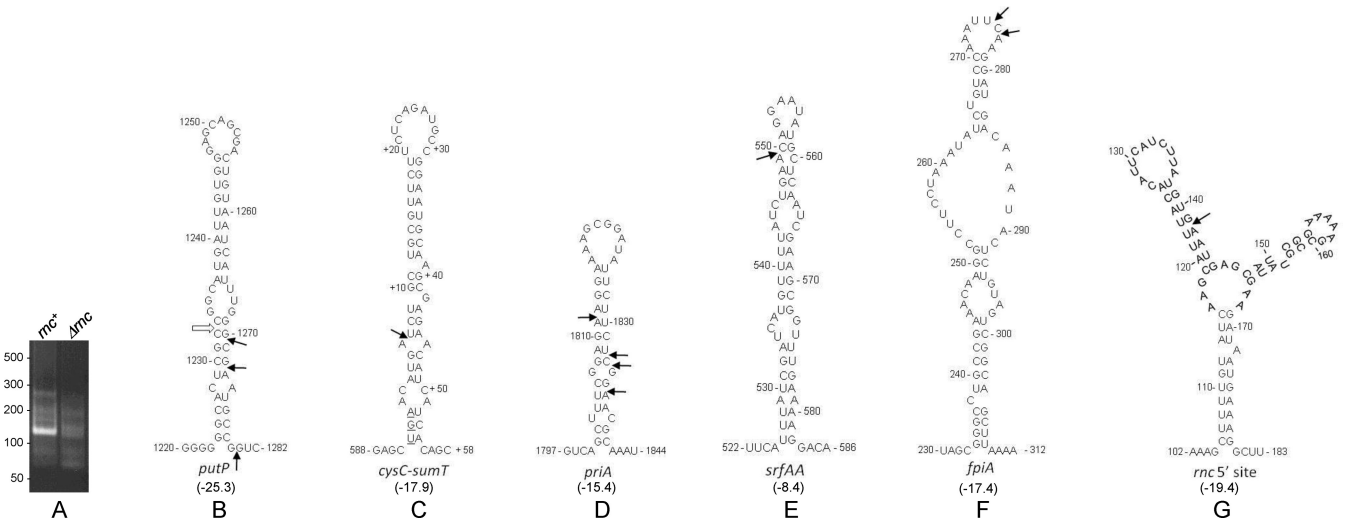

Figure 2. 5′ RLM-RACE mapping of RNase III cleavage sites. (**A**) 5′ RLM-RACE amplification products for mapping *putP* 5′ end generated by RNase III. A PCR product of the expected size is observed only in the *rnc*$^+$ strain. (**B**–**G**) Predicted structures of RNA regions initially identified by PARE analysis to contain RNase III cleavage sites. The structures with the lowest predicted free energy are shown. Values in kilocalories/mol are given in parentheses below each structure. 5′ ends mapped by RLM-RACE are indicated by arrows. Open arrow in Figure 2B indicates the 5′ end of a fragment observed by PARE and Northern blot data but not mapped by RLM-RACE (see text).

Table 4. 5′-RACE mapping of RNase III cleavage sites

Gene	CDS	PARE peak (approximately)	5′-RACE colonies	Genome location
putP	347 150→348 571	348 421	1 of 4	348 420
			2 of 4	348 422
			1 of 4	348 429
cysC-sumT	1 633 369→1 633 962	1 633 979	4 of 4	1 633 969
	1 634 061→1 634 834			
fpiA (*yclQ*)	435 036→435 989	435 313	1 of 4	435 310
			3 of 4	435 311
priA	1 644 068→1 646 485	1 645 900	4 of 11	1 645 878
			2 of 11	1 645 900
			1 of 11	1 645 901
			4 of 11	1 645 903
srfAA	376 968→387 731	377 519	5 of 5	377 518
rnc	1 665 710→1 666 459	1 665 851	6 of 6	1 665 851

such 3′-proximal PARE peaks for many transcription units, and this is explored further below.

Northern blot analysis using a 3′-proximal *putP* oligonucleotide probe was performed on RNA isolated from *rnc*$^+$ and Δ*rnc* strains grown in the presence of 1 mM proline, an inducing concentration for the *putBCP* operon. Because the absence of RNase J1 causes a severe slowing of growth rate (Table 2), all Northern blot analyses were done in the *rnjA*$^+$ background. In the *rnc*$^+$ strain a ∼1.6 kb band was detected (Figure 3C, lane 1), which is the predicted size of a transcript starting at the *putC* internal promoter and ending at the predicted Rho-independent transcription terminator. This *putP* transcript was also observed in a previous report on *put* operon transcription (47). The full-length *putBCP* transcript (∼4 kb) is also detectable in the *rnc*$^+$ strain. An additional small band in the ∼200-nts range was observed in the *rnc*$^+$ strain only; thus, it is likely the predicted downstream product of RNase III cleavage. The ∼200-nts band detected on the blot from a MOPS-agarose gel was examined in more detail on a blot from a 6% denaturing polyacrylamide gel (Figure 3D, lane 1). The results showed two bands of ∼230 and ∼190 nts. The smaller band corresponds well with a fragment extending from the RNase III cleavage site on the downstream side of the *putP* stem-loop structure (Figure 2B) to the transcription termination site. The larger band is likely the result of RNase III cleavage only on the upstream side of the stem loop structure, for which a PARE peak is visible (Figure 3B) but which had fewer than 100 reads/base and so was not included in Table 3. Although RLM-RACE mapping only detected the downstream 5′ end, the Northern blot data suggest that there are RNase III cleavage sites on either side of the stem-loop shown in Figure 2B, as indicated on the figure.

In the Δ*rnc* strain, the *putP* transcript was present in ∼15-fold excess over the *rnc*$^+$ strain (Figure 3B, lane 2; average of two experiments). To explain the difference in *putP* transcript levels, we first looked at mRNA half-life. The rifampicin experiment in Figure 3E demonstrated a difference in *putP* mRNA half-life between the two strains; 13.9 min in the *rnc*$^+$ strain and 23.9 min in the Δ*rnc* strain (av-

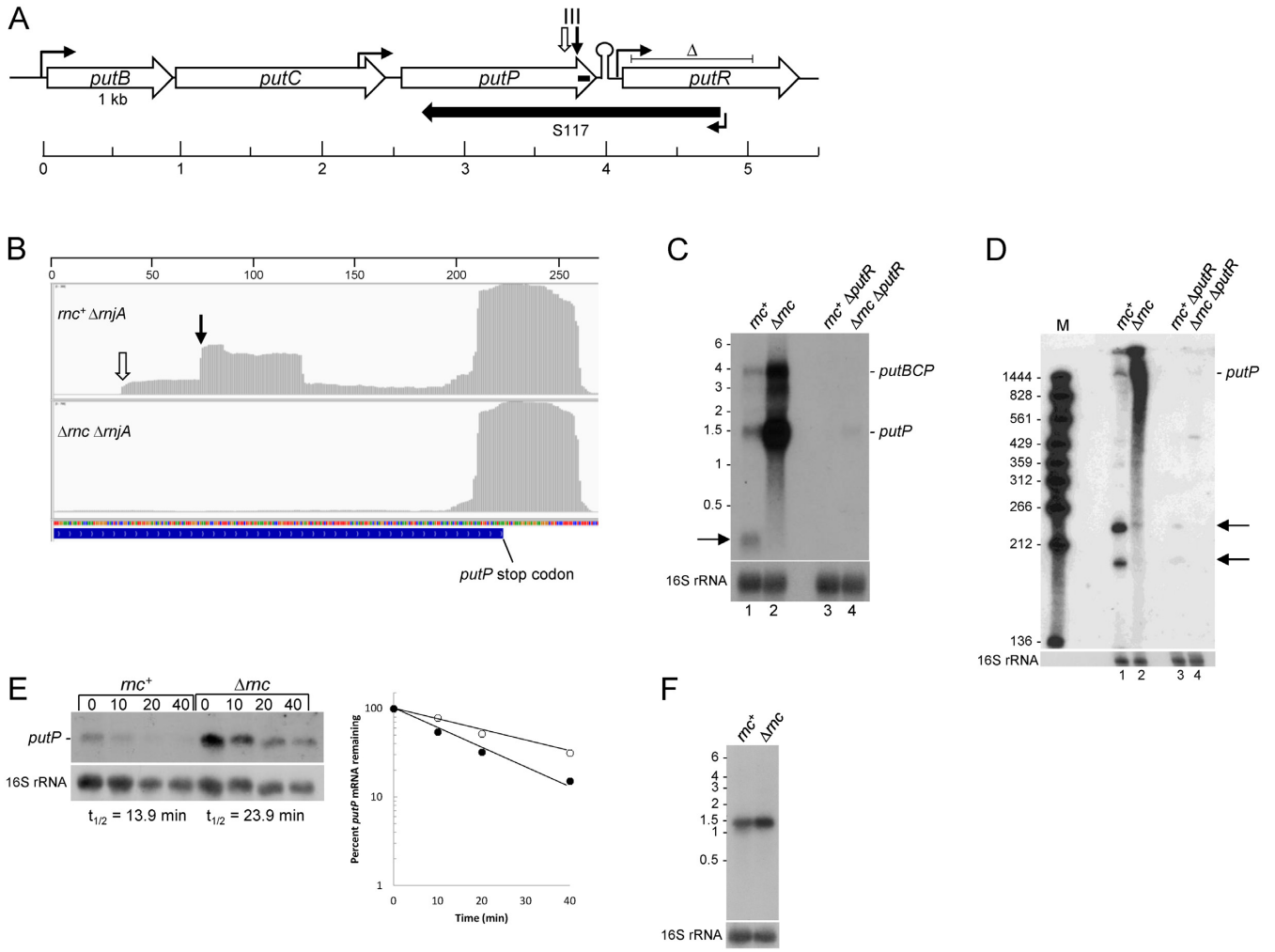

Figure 3. *putP* mRNA. (**A**) Schematic of the *putBCP* operon and regulatory *putR* gene. CDSs are indicated by rightward open arrows, drawn to scale. Sites of upstream regulated promoter and constitutive internal *putC* promoter and *putR* promoter are indicated by hooked arrows. Transcription terminator structure is indicated by a stem-loop. Sites of RNase III cleavage are shown by the downward arrows, as in part B. Extent of S117 antisense RNA is shown by the leftward solid arrow. Extent of the *putR* deletion is indicated by the 'delta' symbol above the *putR* schematic. Horizontal scale indicates distance (in kb). (**B**) Integrated genome viewer image from 3′ end of *putP* CDS in *rnc*$^+$ Δ*rnjA* and Δ*rnc* Δ*rnjA* strains. Site of RNase III cleavage confirmed by 5′ RLM-RACE indicated by the downward arrow. Site of RNase III cleavage inferred from Northern blot analysis indicated by the downward open arrow. Numbers on horizontal scale are nucleotides. (**C**) Northern blot analysis of *putBCP* operon RNA in *rnc*$^+$ and Δ*rnc* strains. The blot is of a MOPS-agarose gel, probed with a 5′-end labeled oligonucleotide complementary to *putP* CDS 1345–1370 nts (indicated by small bar in *putP* CDS in Figure 3A). Migration of *putBCP* operon RNA and *putP* mRNA indicated on the right. Product of RNase III cleavage indicated on the left by the arrow. Migration of unlabeled RNA size markers (kb) indicated on the left. Lanes 1–2 in wild-type *putR* strain; lanes 3–4 in Δ*putR* strain. (**D**) Northern blot analysis of *putP* mRNA cleavage by RNase III. Blot is of a 6% denaturing polyacrylamide gel, probed with the same oligonucleotide probe as in part C. Marker lane (M) contained 5′-end-labeled fragments of a TaqI digestion of plasmid pSE420 (66). Migration of *putP* mRNA and RNase III cleavage products (arrows) indicated on the right. (**E**) Northern blot analysis of *putP* mRNA half-life. Above each lane is the time (min) after rifampicin addition. The blot was probed with the same 5′-end labeled oligonucleotide as in part C. Half-life quantitation shown in graph at right: closed circles, *rnc*$^+$; open circles, Δ*rnc*. (**F**) Northern blot analysis of *putP* RNA transcribed from the P_{spac} promoter. The probe was an oligonucleotide probe complementary to the *lacO* sequence. Migration of unlabeled RNA size markers indicated on the left.

erage of two experiments). This difference was not great enough to explain the ∼15-fold difference in *putP* transcript at steady state. We therefore considered whether the absence of RNase III might have a positive effect on transcription from the *putP* promoter located in *putC*, although the sequence of this promoter suggests it is a Sigma A-dependent promoter and not subject to regulation (45,47). The *putP* CDS and transcription terminator were cloned downstream of a P_{spac} promoter and integrated into the *amyE* locus. The results in Figure 3F show that under control of the exogenous promoter, there was a 1.9-fold difference in *putP* RNA levels in the *rnc*$^+$ and Δ*rnc* strains (average of two experiments), reflecting the half-life difference, as shown in Figure 3E. These results suggest that the 15-fold increase in *putP* RNA in the Δ*rnc* strain arises from both a direct effect on mRNA half-life due to the absence of RNase III cleavage and an indirect, transcriptional effect.

Finally, *putP* was one of only a few RNase III targets for which an overlapping antisense RNA has been mapped (43) (Table 3). As shown in Figure 3A, the S117 antisense RNA

is transcribed from a promoter located in the *putR* CDS, and extends well into the *putP* CDS. To test whether the S117 RNA was required for RNase III cleavage, the pattern of *putP* mRNA was analyzed in a strain that had an internal *putR* deletion that included the S117 promoter and 5′ portion of the S117 transcript (Figure 3A) (47). Deletion of *putR* had a strong negative effect on *putP* mRNA levels (Figure 3C, lanes 3 and 4), for reasons that remain to be determined. Nevertheless, the results in Figure 3D, lanes 1 and 3, show that RNase III cleavage occurred at the same sites in the presence or absence of S117 RNA transcription, suggesting that the structure recognized by RNase III is intramolecular and not formed by intermolecular base-pairing.

srfA operon

A prominent PARE peak with a relatively high RR value of 36.7 was identified in the *srfAA* gene, the first gene in the large 27-kb *srfAABCD* operon that is responsible for *B. subtilis* surfactin production (Figure 4A, Table 3). The cleavage site was mapped by PARE to 551 nts of the *srfAA* CDS and confirmed by 5′ RLM-RACE sequencing, which revealed a 5′ end 1 nt away at 550 (Figure 2E, Table 4). The effect on *srfA* operon RNA was analyzed by Northern blot analysis, using an *srfAA* 5′-proximal oligonucleotide probe on RNA isolated from *rnc*$^+$ and Δ*rnc* strains (Figure 4B). Specific bands could not be resolved, likely because the very long operonic RNA is terminated and processed at many sites. Nevertheless, the absence of RNase III resulted in a large increase (∼3.9-fold) in the level of *srfA* operon RNA in the Δ*rnc* strain relative to the *rnc*$^+$ strain (Figure 4B; sum of signal from the entire lane). These results suggested that cleavage by RNase III reduces the level of *srfA* operon mRNA. Because of the indistinct band pattern for *srfA* operon RNA, we could not reliably perform a half-life measurement in the *rnc*$^+$ and Δ*rnc* strains.

A drop-collapse assay, which detects surfactin in a cell lysate by the reduction of surface tension in a water droplet, was used to determine whether the increased level of *srfAA* RNA in the RNase III mutant had a biological effect. Because the *B. subtilis* 168 strain that was the host strain in these studies is not capable of synthesizing surfactin (*sfp* genotype), *rnc*$^+$ and Δ*rnc* strains were created that were *sfp*$^+$ (see 'Materials and Methods' section). The qualitative surfactin assay shown in Figure 4C indicated an increased level of surfactin in the medium of the strain lacking RNase III. A semi-quantitative assay of surfactin levels (data not shown; see 'Materials and Methods' section) gave approximately a 2-fold increase in surfactin levels in the absence of RNase III. Thus, these results suggest that RNase III is involved, directly or indirectly, in limiting the amount of surfactin in the medium.

The *srfA* operon is also involved in the development of competence (48), which is due to the presence of the *comS* gene embedded in the *srfAB* CDS, the second gene in the *srfA* operon (49). ComS protein functions to release the ComK transcription factor from an inactive complex, triggering competence development (50). Thus, it was possible that increased *srfA* RNA in the Δ*rnc* strain might affect competence, as well. However, experiments showed no significant difference in competence levels between *rnc*$^+$ and Δ*rnc* strains (data not shown).

rnc autoregulation

Based on Northern blot analysis in this study (see below), the *rnc* gene is likely to be the second gene in a ∼6 kb operon consisting of *acpA* (acyl carrier protein), *rnc*, *smc* (involved in chromosome condensation and segregation) and *ftsY* (a signal recognition particle protein). A predicted Rho-independent transcription terminator sequence is present immediately downstream of the *rnc* stop codon, suggesting that an *acpA-rnc* mRNA is also synthesized (Figure 5A). Two PARE peaks were mapped to the *rnc* gene itself in the *rnc*$^+$ strain, at around 140 and 650 nts of the CDS (Figure 5A). As the *rnc* mutant strain used for the PARE protocol was a deletion strain that was missing the entire *rnc* CDS, there was no comparable PARE data from the Δ*rnc* strain to determine whether these peaks were due to RNase III cleavage. Since RNase III autoregulation of *rnc* mRNA has been reported in other organisms (22,24,51), we followed up the data from the *rnc*$^+$ strain by creating a strain that contained the *rnc* gene with an E138A mutation at the enzyme active site. Such a mutation in the homologous residue of the *E. coli* enzyme (position 117) results in loss of cleavage activity (52). Indeed, we observed that scRNA processing was completely absent in the strain carrying the E138A mutation (data not shown). Northern blot analysis of the *rnc*$^+$ strain, using an oligonucleotide probe targeted to a sequence in the *rnc* CDS, did not detect a clear full-length *acpA-rnc-smc-ftsY* operon mRNA (Figure 5B, lane 1). Approximately 1.1 kb *acpA-rnc* mRNA was detected, which was the expected size from the putative *acpA* promoter to the predicted transcription terminator following *rnc*. In addition, a band of unknown origin was detected running at ∼2 kb. In the RNase III *E138A* mutant strain, full-length operon mRNA was easily detected, as well as ∼16-fold increase in *acpA-rnc* mRNA (Figure 5B, lane 2). The result suggested an autoregulation of RNase III by cleavage of its own mRNA. A rifampicin experiment to determine mRNA half-life showed that *acpA-rnc* mRNA is short-lived in the *rnc*$^+$ strain ($t_{1/2} = 3.2$ min) and relatively long-lived in the Δ*rnc* strain ($t_{1/2} = 11.6$ min) (Figure 5C). The large increase in *acpA-rnc* mRNA in the strain lacking RNase III is likely due to effects on both transcription and mRNA stability, as we found for *putP* mRNA.

rrn operon RNA processing in the *rnc* strain

Besides scRNA, the other molecule for which RNase III cleavage was previously documented is ribosomal RNA (cf. schematic in Figure 6A). Although mature rRNA is removed prior to PARE analysis (see 'Materials and Methods' section), RNA fragments that contain sequences upstream and downstream of mature rRNA are captured. Because the growth rate of the *rnc*$^+$ and Δ*rnc* strains was nearly identical (Table 2), we did not expect there to be significant differences in transcription levels of *rrn* operons between the two strains. In addition, similar results from the different *rrn* operons indicated that there was no differential depletion of specific *rrn* operon RNAs. *B. subtilis* contains

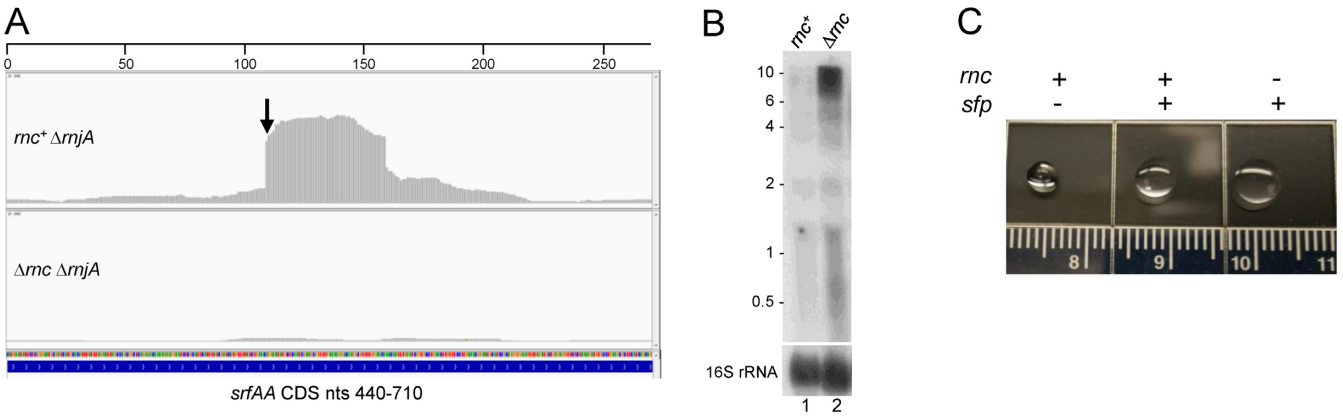

Figure 4. *srfAA* mRNA. (**A**) Integrated genome viewer image from 440–710 nts of the *srfAA* CDS, in *rnc*$^+$ Δ*rnjA* and Δ*rnc* Δ*rnjA* strains. 5′ end of the downstream product of RNase III cleavage confirmed by 5′ RLM-RACE is indicated by the downward arrow. Numbers on horizontal scale are nucleotides. (**B**) Northern blot analysis of steady-state *srfA* operon RNA in *rnc*$^+$ and Δ*rnc* strains. The probe was a 5′-end labeled oligonucleotide complementary to 167–195 nts of the *srfAA* CDS. Migration of unlabeled RNA size markers indicated on the left. (**C**) Drop collapse assay. *rnc* and *sfp* genotypes are indicated above each drop photo.

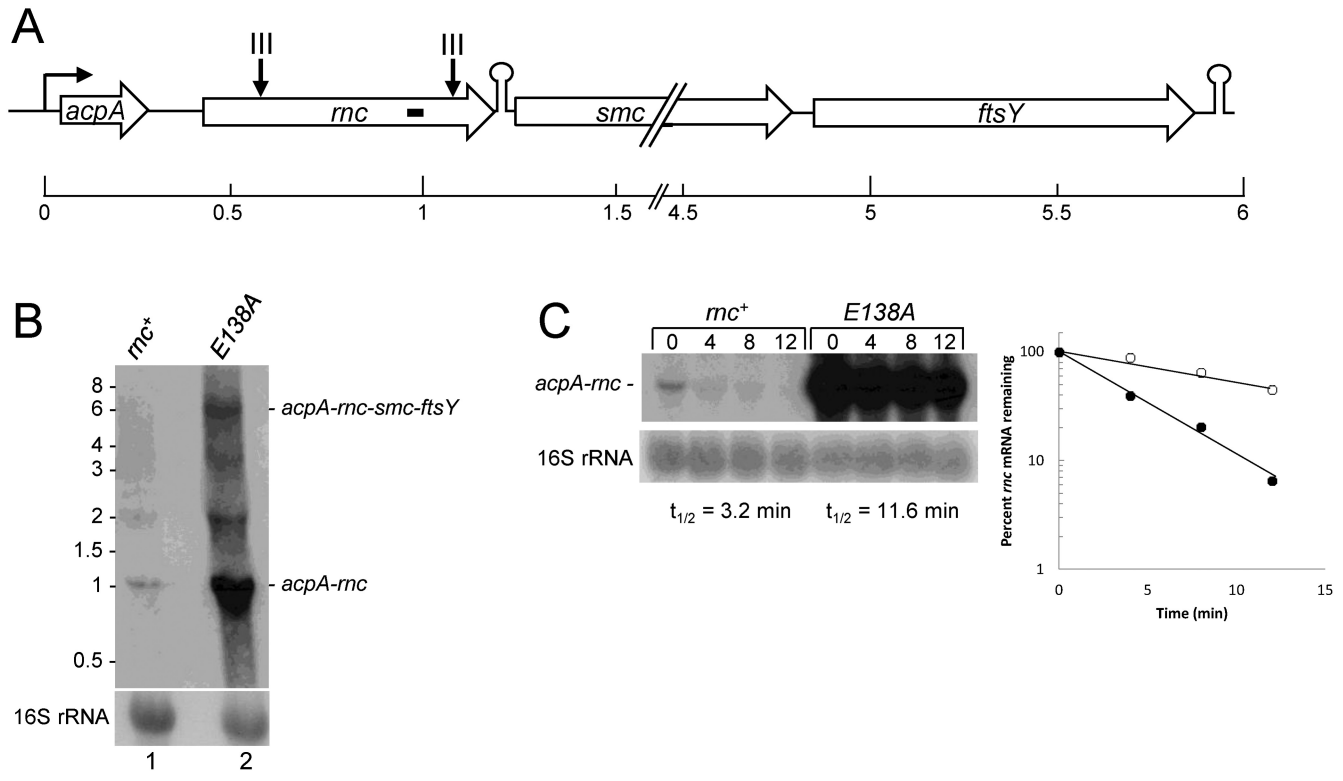

Figure 5. *rnc* mRNA. (**A**) Schematic diagram of *acp* operon. Representations are as in Figure 3A. (**B**) Northern blot analysis of steady state *rnc* operon RNA in *rnc*$^+$ and *E138A* strains. The probe was a 5′-end labeled oligonucleotide complementary to 533–553 nts of the *rnc* CDS (indicated by small bar in *rnc* CDS in Figure 5A). Migration of full-length operon RNA and *acpA-rnc* mRNA indicated on the right. Migration of unlabeled RNA size markers indicated on the left. (**C**) Northern blot analysis of *rnc* mRNA half-life. The probe was the same probe as in part B. Above each lane is the time (min) after rifampicin addition. Half-life quantitation shown in graph at right: closed circles, *rnc*$^+$; open circles, Δ*rnc*.

10 *rrn* operons with differing rRNA/tRNA gene organization; we focused on *rrnA*. Identical results were obtained for the *rrnO* operon (data not shown), which has the same rRNA/tRNA structure as *rrnA*. In the Δ*rnc* mutant strain only, a major PARE peak was observed starting near the P2 promoter TSS (Figure 6B, peak 1) (53). We speculate that RNA transcribed from the upstream P1 promoter is subject to endonuclease cleavage, yielding a 5′ end that is around the P2 TSS. The P2 TSS PARE peak is not detected in the *rnc*$^+$ strain, perhaps because RNase III cleavage in the 16S processing stalk (site III-1) is followed by 3′ exonuclease activity to degrade the precursor 5′ fragment. A peak similar to peak 1, located near the proximal *rrn* promoter, was observed for all *rrn* operons (data not shown).

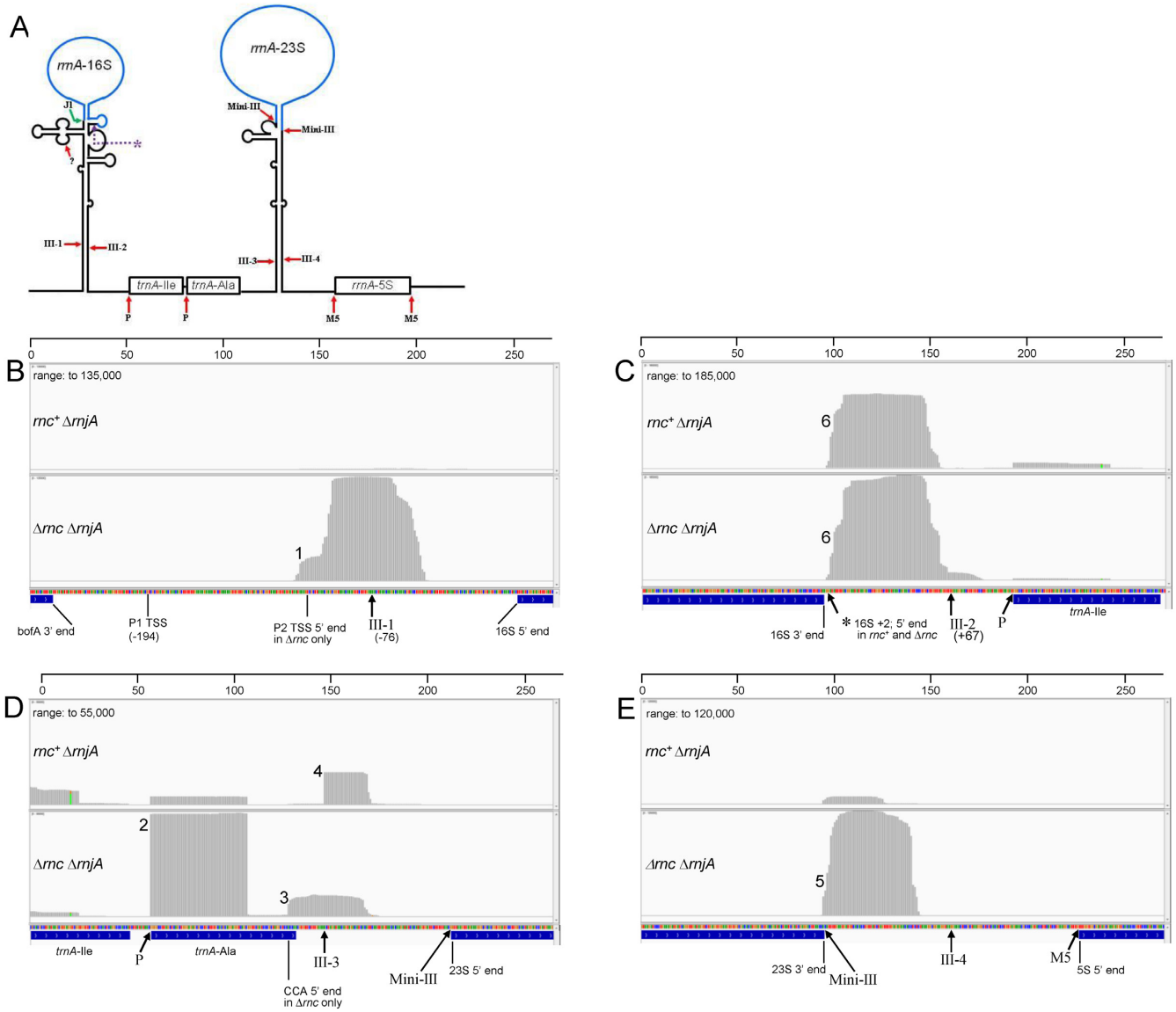

Figure 6. PARE analysis of ribosomal RNA. (**A**) Schematic diagram of *rrnA* precursor RNA secondary structure and endonucleases involved in rRNA and tRNA maturation. Mature 16S and 23S rRNA in blue. Red arrows point to sites of endonuclease cleavage: III, RNase III; P, RNase P; M5, RNase M5; ?, unknown endonuclease. 16S 5′-end maturation occurs by 5′ exonuclease activity of RNase J1 (hooked green arrow). Endonuclease involved in 16S 3′ end maturation discovered in this study indicated by purple asterisk and dotted line. (**B**–**E**) Integrated genome viewer images of *rrnA* region in *rnc*$^+$ Δ*rnjA* and Δ*rnc* Δ*rnjA* strains, in chromosomal order from upstream of the 16S rRNA sequence (B) to the start of the 5S rRNA sequence (E). Numbers on horizontal scale are nucleotides. The start and end point of mature rRNA and tRNA sequences are labeled below each panel. Arrows point to sites of endonuclease cleavage. Sites of RNase III cleavage are numbered as in part A. The data range was adjusted to show maximum peak heights, and the maximum range is indicated at the top left of each panel. Peaks that are described in the text are numbered 1–6. The site of endonuclease cleavage involved in 16S 3′ end maturation is indicated by the asterisk in part C.

The PARE protocol also revealed peaks that began precisely at the 5′ end of some tRNAs. Two tRNAs (Ile and Ala) are present between 16S and 23S rRNA in the *rrnA* operon (Figure 6A). The PARE peak representing the 5′ end of *trnA*-Ala was present at a 12–13-fold higher level in the Δ*rnc* strain compared to the *rnc*$^+$ strain (Figure 6D, peak 2). A similar result was observed for glycyl tRNA (data not shown). Since the five Ala tRNA genes in rRNA operons have the same sequence, and the mapping program does not distinguish between them, it is not clear whether all Ala tRNAs or only one or several is accumulating in the absence of RNase III. This is not likely to be due to differential selection of tRNAs in the total RNA isolated from the *rnc*$^+$ and Δ*rnc* strains, since the relative levels of the PARE peak at the 5′ end of *trnA*-Ile (Figure 6C, right; Figure 6D, left) were inversely related (∼4-fold higher in the *rnc*$^+$ strain). We have no explanation for why alanyl and glycyl tRNA accumulate to such a relatively high degree in the Δ*rnc* strain. In addition, we observed in the Δ*rnc* strain a significant PARE peak beginning 3 nts from the 3′ end of *trnA*-Ala (Figure 6D, peak 3). tRNA-Ala ends with a CUCCA↓CCA sequence (downward arrow is the start of the PARE peak),

of which the CUCC residues base pair with 4 G's at the 5′ terminus of the tRNA. This 3′ tRNA sequence does not conform to the known substrate requirements for RNase Z (54), and it is not clear why cleavage to remove the encoded CCA sequence would occur, if restoration of the same CCA is required for tRNA function.

Note that in the *rnc*$^+$ strain, the 5′ end that is due to RNase III cleavage in the upstream portion of the 23S stalk (site III-3) is clearly visible as a PARE peak (Figure 6D, peak 4). As the mature 5′ end of 23S rRNA is determined by Mini-III cleavage (18), this peak likely represents an RNA fragment that extends from the RNase III-3 cleavage site to the Mini-III cleavage site (see Figure 6A). Accumulation of this fragment is relatively low, likely due to 3′ exonucleolytic degradation.

A PARE peak beginning immediately downstream of the mature 23S rRNA sequence was detected in both strains, but was present at a 14-fold higher level in the Δ*rnc* strain (Figure 6E, peak 5). This is likely the 5′ end of a fragment that extends from the Mini-III cleavage site — which yields the mature 23S rRNA 3′ end — to the 5′ end of 5S rRNA, which is generated by RNase M5 (see Figure 6A) (55). In the Δ*rnc* strain, the absence of RNase III cleavage at the III-4 site, in between the Mini-III and RNase M5 cleavage sites, likely stabilizes this fragment.

Direct evidence for endonuclease cleavage close to the 16S rRNA 3′ end

A prominent PARE peak was detected in both *rnc*$^+$ and Δ*rnc* strains beginning 2-nts downstream of the 3′ end of mature 16S rRNA (Figure 6C, peak 6). This peak begins 65-nts upstream of the RNase III cleavage site (site III-2) in the downstream part of the 16S stalk (Figure 7A). Northern blot analysis using a probe directed to the 16S stalk sequence upstream of the RNase III-2 cleavage site revealed a smear of RNA fragments 65 nts and shorter that was clearly observed in an *rnjA* mutant strain and more faintly in the wild-type strain (Figure 7B, lanes 1 and 2). The 65-nts fragment is hypothesized to extend from an endonuclease cleavage site located 2-nts downstream of the 3′ end of 16S rRNA to the RNase III-2 cleavage site. Presumably, RNase J1 degrades this fragment rapidly from its unprotected 5′ end, which is why it is much less prominent in the wild-type strain. Since the PARE data was derived from *rnc*$^+$ and Δ*rnc* strains that were also deleted for *rnjA*, the PARE peak representing this fragment is present in abundance in Figure 6C. The 65-nts fragment was also visible faintly in the *rny* mutant strain (Figure 7B, lane 3). We have obtained preliminary PARE data also from the *rny* strain (not shown), and the same PARE peak is present beginning 2-nts downstream of 16S rRNA, confirming that the endonuclease cleavage is not catalyzed by RNase Y. A larger fragment of ∼82 nts was detected in the Δ*rnc* strain (Figure 7B, lane 4). We hypothesize that this fragment extends from a site of cleavage 2-nts downstream of 16S rRNA to the base of the 16S stalk. For *rrnA* and *rrnO* operons, in which 16S rRNA is followed by tRNA-Ile, the 3′ end of this fragment would be generated by RNase P cleavage at the 5′ end of tRNA-Ile, followed by 3′ exonuclease chewing back to the base of the 16S stalk (Figure 7A). For all other operons, where 16S rRNA is followed by 23S rRNA, the 3′ end of this fragment may be generated by endonuclease cleavage (possibly RNase Y) in the single-stranded region between the 16S and the 23S processing stalk, followed by 3′ exonuclease chewing back to the base of the 16S stalk (Figure 7A).

Confirmation of the 5′ end of the 65-nts fragment was obtained by primer extension and 5′ RACE mapping. In Figure 7C, the largest of the specific primer extension products mapped to 2-nts downstream of 16S rRNA. This product is present in much higher abundance in the strains missing RNase J1 (Figure 7C, lanes 3 and 4). Shorter primer extension products may be due to imprecise endonuclease cleavage, which would not be detected in the PARE analysis. 5′ RACE mapping was done on an RNA ligation product between the 65-nts fragment and 5S rRNA (Figure 7D). Sequencing across the junction revealed the same 5′ end, located 2-nts downstream of 16S rRNA. Taken together, these data have revealed that 16S rRNA 3′ end maturation likely involves cleavage by an unknown endonuclease 2-nts downstream of the 16S rRNA sequence, followed by 3′ exonucleolytic trimming to yield the mature 16S rRNA.

Decay of 3′-proximal RNA fragments is highly RNase J1-dependent

In the course of examining PARE peaks that were likely sites of RNase III cleavage, we noticed that a large number of genes had a PARE peak near the end of the CDS; see Figure 3B for an example. As explained above, the *rnc*$^+$ and Δ*rnc* strains used for the PARE analysis were also deleted for the *rnjA* gene encoding the 5′ exonuclease RNase J1. We hypothesized that the 3′-terminal PARE peaks were the result of an absence of RNase J1, which is responsible for turnover of fragments containing the transcriptional terminator sequence. Previous work on individual RNAs had indicated such a role for RNase J1 (38). A PARE analysis was also done on a P_{spac}-*rnjA* strain that had the *rnjA* gene transcribed under the control of the IPTG-inducible P_{spac} promoter. Expression of *rnjA* driven by the P_{spac} promoter has been shown in earlier studies to result in 5-fold less *rnjA* mRNA and RNase J1 protein than when *rnjA* is expressed from its native promoter (5,56). (A PARE analysis in a strain containing wild-type *rnjA* has not been performed.) The PARE analyses from these strains provided an opportunity to assess the contribution of RNase J1 to global turnover of 3′-proximal RNA decay intermediates. Genes that were either monocistronic or the last gene in an operon were predicted to show an accumulation of 3′-proximal PARE reads in an *rnjA* deletion strain. The data in Table 5 show the number of genes with PARE peaks that either contained the stop codon or that began after the stop codon but before the following CDS. In the strain that was deleted for *rnjA*, greater than half of monocistronic genes and last genes in an operon (54.8 and 54.5%, respectively) showed a PARE peak in the area of the stop codon. The percentages of monocistronic genes and last genes in an operon that showed 3′-proximal PARE peaks were reduced about 2-fold in the P_{spac}-*rnjA* strain grown in the presence of IPTG and containing a low level of RNase J1 (26.7 and 31.8%, respectively). On the other hand, for genes located elsewhere in operons, only 14–15% showed a 3′-proximal PARE peak.

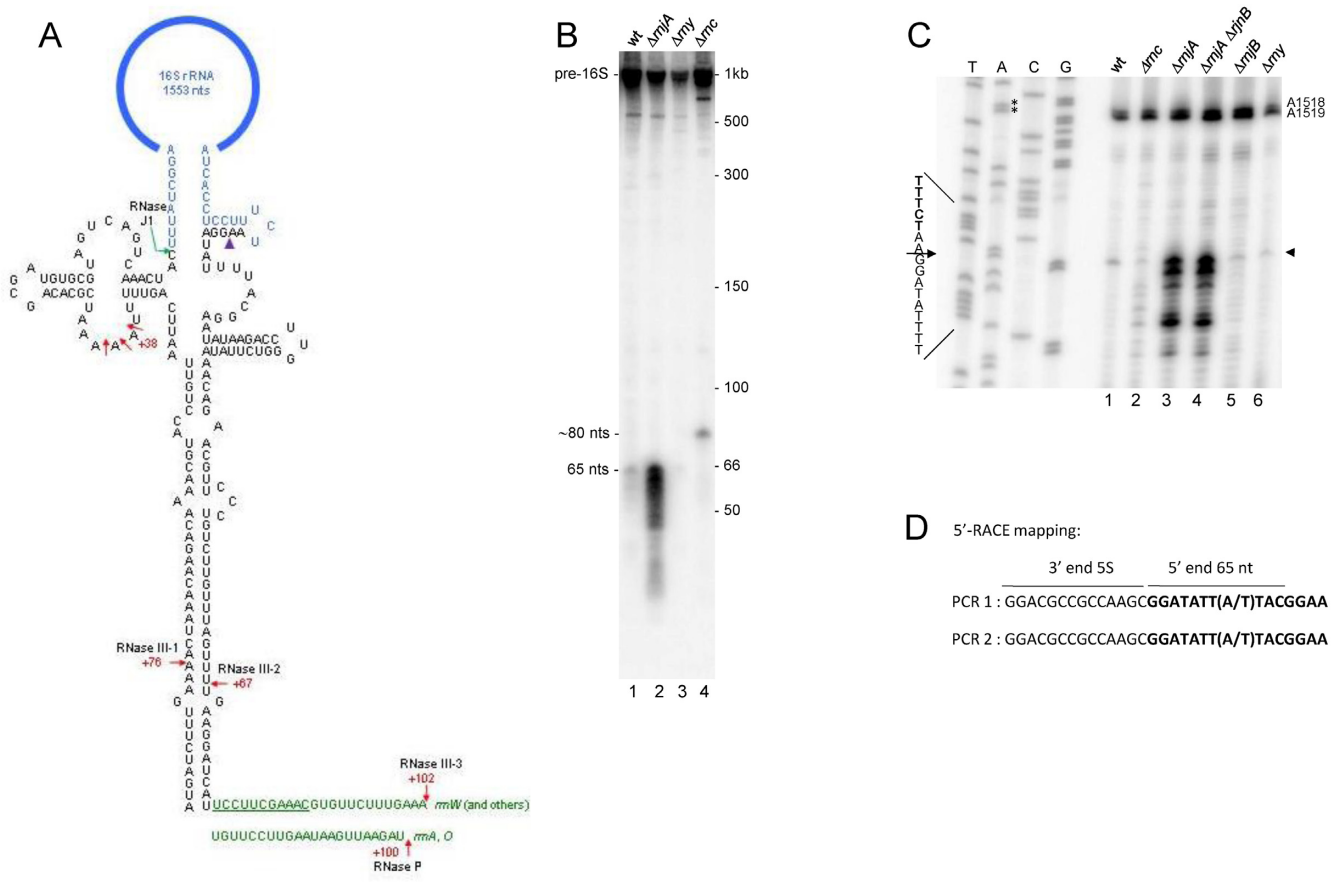

Figure 7. (**A**) Details of 16S processing stalk. The sequence for the *rrnW* stalk is shown. Mature 16S rRNA sequences are in blue. Numbering is the distance from the mature 5′ or 3′ ends of 16S rRNA. Sites of previously known endonuclease cleavage are indicated by red arrows. RNase J1 processing of 16S rRNA 5′ end is indicated by the green hooked arrow. Site of endonuclease cleavage discovered in this study is indicated by the purple arrowhead. Sequence downstream of the stalk (in green) is shown for *rrnW* and other operons (top) and for *rrnA* and *rrnO* (bottom). For *rrnW* and other operons, the 16S sequence is followed by the 23S sequence. The underlined sequence is the single-stranded region between the 16S and 23S processing stalks, which may be the target of RNase Y endonuclease cleavage. For the *rrnA* and *rrnO* operons, the 16S sequence is followed by two tRNAs (cf. Figure 6A), whose 5′ end is matured by RNase P cleavage. (**B**) Northern blot analysis of 16S rRNA 3′ fragment, using an oligonucleotide probe complementary to a sequence immediately upstream of the RNase III cleavage site (III-2) in the 16S stalk. Relevant genotype of strains indicated above each lane. Strains used for experiments in Figure 7 are the 'CCB' strains listed in Table 1. Migration of precursor 16S rRNA and processed fragments indicated on the left. Migration of unlabeled RNA markers (nts) shown on the right. (**C**) Primer extension assay for 5′-end mapping of the 65-nts fragment in the indicated ribonuclease mutant strains. Control sequencing lanes of an rDNA fragment are the leftmost lanes. For ease of reading, the sequence readout is written as the reverse complement. Major 5′ end indicated by arrowhead on right. Strong stops at A1518 and A1519 are due to methylation of these residues by KsgA (67). (**D**) 5′-RACE mapping of the 65-nts fragment. The 65-nts fragment was ligated to 5S rRNA present in total RNA and reverse transcriptase-PCR was performed across the junction. Boldface sequence is from the 65-nts fragment 5′ end. In different operons, the eighth residue is either A or T.

Importantly, for this latter category there was no significant difference in the percent of genes with a 3′-proximal PARE peak between the strain with no RNase J1 and the strain with low RNase J1 (14.5 and 14.7%, respectively; Table 5). These results strongly support the hypothesis that RNase J1 is globally involved in the turnover of 3′-terminal fragments.

DISCUSSION

In this report, a comparison of endonuclease cleavage sites in *B. subtilis* strains containing or missing the *rnc* gene allowed mapping of RNase III cleavage sites in multiple RNAs. The list of 53 CDS and 5 intergenic RNase III targets in Table 3 likely represents a subset of the actual RNase III cleavages in the transcriptome. We used stringent criteria to differentiate RNAs that are direct RNase III targets from RNAs that are downregulated transcriptionally in the *rnc* strain (see description of the RR value in 'Results' section). It is likely that other genes for which we observed PARE peaks, but which did not conform to the criteria used, are also RNase III targets. Another factor that probably limited the number of genes identified as RNase III targets was that the PARE protocol depends on ligation of a 5′ adaptor to a monophosphorylated end, which may not be efficient depending on the potential for RNA folding at the 5′ end. Thus, our findings suggest that, in addition to processing of the stable RNAs, scRNA and rRNA, many mRNAs are subject to RNase III cleavage. A similar conclusion was arrived at in studies of RNase III targets in other organisms (24,27,29,30,57). The Sim *et al.* study (57) employed *E. coli* strains with tunable RNase III expression rather than a knockout strain in order to avoid indirect effects of loss of

Table 5. 3′-proximal PARE peaks

Gene category	Number of genes[a]	Number of genes with 3′-proximal peak (percent)	
		Δ*rnjA* strain	P_{spac}-*rnjA* strain
Known operonic location[b]	1562	608 (38.9)	360 (23.0)
Monocistronic	622	341 (54.8)	166 (26.7)
Last in operon	327	178 (54.5)	104 (31.8)
Not monocistronic, not last in operon	613	89 (14.5)	90 (14.7)

[a]Genes with >1 read/base in a standard RNA-Seq analysis in either strain.
[b]Based on BsubCyc transcription unit information.

RNase III, and they found a total of 87 upregulated and 100 downregulated genes that were apparently direct targets of RNase III.

In the *S. aureus* studies cited above (24,30), RNase III cleavage was found most often to be associated with antisense RNAs, suggesting that double-stranded RNA targets were formed by intermolecular base-pairing. Indeed, the Lasa *et al.* analysis of *B. subtilis* RNAs (30) suggested that this was the case in this organism as well. However, for the target sites mapped in our study, we found little evidence that RNase III targeting required antisense RNA pairing. Only four of the targeted genes were located in a genomic region with known antisense RNAs that overlapped with the cleavage sites (43). We showed that one of these—the S117 antisense RNA that overlaps the *putP* CDS—was dispensable for RNase III cleavage (Figure 3D). Thus, it appears that the overwhelming majority of mapped RNase III targets are formed by intramolecular base-pairing.

Of the six RNase III target sites that were confirmed by 5′ RLM-RACE analysis (Figure 2), a single 5′ end was observed in three of the cases, whereas more than one 5′ end located in the vicinity of the PARE cleavage site were obtained in the other cases (Table 4). It is possible that RNase III cleavage is not precise, and may cleave at more than one residue. Indeed, structural studies of the *Aquifex aeolicus* RNase III by Court *et al*. have recently revealed alternate cleavage sites for a single substrate (13). However, this is apparently uncommon, and is not likely to explain the multiple 5′ ends obtained by 5′ RLM-RACE analysis in our work. Rather, we speculate that additional 5′ exonuclease activities may be present in the *rnjA* deletion strain that 'nibble' at the 5′ ends generated by RNase III cleavage, resulting in additional 5′ ends in some cases.

Two of the fully-mapped RNase III cleavage sites occurred in loop sequences as predicted by mfold (Figure 2). This is not typical of *E. coli* RNase III cleavage sites, as has been studied in detail by Nicholson *et al*. (14). It may be that the predicted structures are not the only ones possible. In addition, the mapped 5′ end may be due to exonucleolytic digestion that occurs after RNase III cleavage. We note that atypical RNase III cleavage sites were also suggested in a study of *S. coelicolor* targets (29). While many studies of model *E. coli* RNase III substrates have yielded rather strict rules for sequence/structure that provide for optimal cleavage, it may be the case that natural substrates have uncharacterized features that make them RNase III targets. It has become clear only in the last few years that many native mRNA CDSs contain RNase III target sites, and therefore these substrates have not been studied yet in detail. In addition, RNase III enzymes from different organisms may have altered specificities, as we showed previously in *in vitro* experiments with purified *E. coli* and *B. subtilis* RNase III enzymes (20). To learn more about the requirements for *B. subtilis* RNase III target site recognition, it will be necessary to analyze by *in vitro* assays several of the natural substrates identified in this study and for which the secondary structure has been confirmed by structure-probing experiments.

For three of the mRNAs that were cleaved by RNase III, we showed an effect on the steady-state levels of mRNA, with much lower levels in the rnc^+ strain. In the case of *putP* and *rnc*, we found that this is only partially a result of an increase in mRNA half-life in the absence of RNase III. For mRNA targets of RNase III, it is likely that modulation of mRNA levels is achieved by a combination of transcriptional and post-transcriptional mechanisms. Lasa *et al.* have suggested that RNase III functions to modulate levels of sense RNAs (30). Whether this occurs solely as a direct consequence of RNase III cleavage will require further investigation of individual mRNAs.

The PARE analysis afforded the opportunity to learn about decay of mRNA fragments that contain the Rho-independent transcription terminator sequence followed by a run of U residues, which are inherently resistant to binding and/or decay by 3′ exonucleases. In organisms that do not contain a 5′ exonuclease, such as *E. coli*, the mechanism for turnover of 3′-end-containing fragments involves polyadenylation at the 3′ end to allow binding and processive decay by RNase R or reiterative binding and decay by PNPase (reviewed in (58)). Based on our observation of increased 3′-end-containing fragments for three RNAs in strains depleted of RNase J1 (38), we hypothesized that organisms that contain a 5′ exonuclease rely on such an activity for the turnover of 3′-terminal fragments. While a significant percentage of *B. subtilis* mRNAs are known to be polyadenylated, even more so than in *E. coli* (59), the *B. subtilis* polyadenylating enzyme has not yet been identified (60), making it impossible to study the role of polyadenylation in mRNA decay. The results in Table 5, which showed a large increase in PARE peaks at 3′ ends of transcripts in the *rnjA* deletion strain, clearly demonstrate the global role that RNase J1 plays in the turnover of 3′-end-containing fragments. Thus, degradation of 3′-terminal fragments for many *B. subtilis* mRNAs likely involves one or more endonuclease cleavages upstream of the stop codon, followed by RNase J1 turnover of the downstream products.

The PARE analysis was revealing as far as 16S rRNA 3′ end maturation is concerned. The mechanism for bacterial 16S rRNA 3′ end maturation has been debated for

years, and is still not resolved, even for the well-studied *E. coli*. In *E. coli*, RNase III cleaves 33-nts downstream of the mature 3′ end. As processing intermediates with <33-nts downstream of the 16S rRNA 3′ end have not been detected, it had been assumed for a long time that the 3′ end of 16S rRNA is generated directly by cleavage catalyzed by an unidentified endonuclease (reviewed in (61)). More recently, evidence for *E. coli* 16S rRNA 3′ end maturation by exonucleolytic trimming has been published (39). These authors found that the absence of multiple 3′ exonucleases results in the accumulation of precursor 16S rRNA with a 33-nts 3′ extension. Similarly, studies in *Pseudomonas syringae* have suggested that RNase R, a 3′ exonuclease, is required for 16S rRNA 3′ end maturation, most likely by chewing back from the site of downstream RNase III cleavage (62). However, another view of 16S rRNA 3′ end maturation has been proposed by Walker *et al*., based on their work with the YbeY protein, a highly conserved bacterial protein whose absence in *E. coli* results in pleiotropic phenotypes. This group showed initially that *ybeY* mutants were defective in processing of all three rRNAs, and *ybeY* mutant strains that carried additional mutations for the 3′ exonucleases RNase R or PNPase had little mature 16S rRNA (63). More recently, the same group showed that YbeY has single strand-specific endonuclease activity (64). These authors suggested that *E. coli* 16S rRNA 3′ end maturation may involve YbeY endonuclease cleavage. Details of 16S rRNA 3′ maturation in *B. subtilis* have not been addressed. We show here by PARE analysis in *rnc*$^+$ and Δ*rnc* strains (Figure 6) and by northern blot and RACE analysis (Figure 7) the first direct evidence for endonuclease cleavage in the final or near-final maturation of *B. subtilis* 16S rRNA. Cleavage occurs 2-nts downstream of the mature 16S rRNA 3′ end, and is presumably followed by exonucleolytic trimming to complete the maturation process. The endonuclease cleavage close to the 16S rRNA 3′ end identified here cannot be due to YbeY, as 5′ ends detected in the PARE must begin with a 5′ monophosphate and YbeY activity leaves a 5′ hydroxyl (64). The fragment extending from the 16S rRNA 3′-proximal endonuclease cleavage site to the RNase III cleavage site (III-2) was barely detectable in the wild-type strain but clearly visible in the *rnjA* deletion strain (Figure 7B), indicating that it is rapidly degraded by RNase J1. It is possible that degradation of the fragment generated from the downstream side of the 16S stalk is required to allow exonucleolytic maturation of the 16S rRNA 5′ end by RNase J1 on the upstream side of the 16S stalk (65). The search for the endonuclease activity responsible for near final maturation of 16S rRNA in *B. subtilis* is ongoing.

ACCESSION NUMBER

Raw PARE data and RNA-Seq data are available at the NCBI GEO database, accession number GSE77217.

SUPPLEMENTARY DATA

Supplementary Data are available at NAR Online.

ACKNOWLEDGEMENT

We thank Boris Belitsky for advice and for the *putR* deletion strain.

FUNDING

National Institutes of Health [GM-100137 to D.H.B.]; CNRS [UMR 8261]; Université Paris VII-Denis Diderot; the Agence Nationale de la Recherche [ANR-12-BSV6-007-asSUPYCO, ANR-11-LABX-0011-01-Dynamo to C.C.]; Department of Scientific Computing at the Icahn School of Medicine at Mount Sinai (in part). Funding for open access charge: National Institutes of Health [GM-100137].
Conflict of interest statement. None declared.

REFERENCES

1. Bechhofer,D.H. (2011) Bacillus subtilis mRNA decay: new parts in the toolkit. *Wiley Interdiscip. Rev. RNA*, **2**, 387–394.
2. Lehnik-Habrink,M., Lewis,R.J., Mader,U. and Stulke,J. (2012) RNA degradation in Bacillus subtilis: an interplay of essential endo- and exoribonucleases. *Mol. Microbiol.*, **84**, 1005–1017.
3. Durand,S., Gilet,L., Bessieres,P., Nicolas,P. and Condon,C. (2012) Three essential ribonucleases-RNase Y, J1, and III-control the abundance of a majority of Bacillus subtilis mRNAs. *PLoS Genet.*, **8**, e1002520.
4. Condon,C. (2010) What is the role of RNase J in mRNA turnover? *RNA Biol.*, **7**, 316–321.
5. Liu,B., Deikus,G., Bree,A., Durand,S., Kearns,D.B. and Bechhofer,D.H. (2014) Global analysis of mRNA decay intermediates in Bacillus subtilis wild-type and polynucleotide phosphorylase-deletion strains. *Mol. Microbiol.*, **94**, 41–55.
6. Piton,J., Larue,V., Thillier,Y., Dorleans,A., Pellegrini,O., Li de la Sierra-Gallay,I., Vasseur,J.-J., Debart,F., Tisne,C. and Condon,C. (2013) Bacillus subtilis RNA deprotection enzyme RppH recognizes guanosine in the second position of its substrates. *Proc. Natl. Acad. Sci. U.S.A.*, **110**, 8858–8863.
7. Hsieh,P.-K., Richards,J., Liu,Q. and Belasco,J.G. (2013) Specificity of RppH-dependent RNA degradation in Bacillus subtilis. *Proc. Natl. Acad. Sci. U.S.A.*, **110**, 8864–8869.
8. Figaro,S., Durand,S., Gilet,L., Cayet,N., Sachse,M. and Condon,C. (2013) Bacillus subtilis mutants with knockouts of the genes encoding ribonucleases RNase Y and RNase J1 are viable, with major defects in cell morphology, sporulation, and competence. *J. Bacteriol.*, **195**, 2340–2348.
9. Richards,J., Liu,Q., Pellegrini,O., Celesnik,H., Yao,S., Bechhofer,D.H., Condon,C. and Belasco,J.G. (2011) An RNA pyrophosphohydrolase triggers 5′-exonucleolytic degradation of mRNA in Bacillus subtilis. *Mol. Cell*, **43**, 940–949.
10. Bechhofer,D.H. (2013) Nucleotide specificity in bacterial mRNA recycling. *Proc. Natl. Acad. Sci. U.S.A.*, **110**, 8765–8766.
11. Deana,A. and Belasco,J.G. (2005) Lost in translation: the influence of ribosomes on bacterial mRNA decay. *Genes Dev.*, **19**, 2526–2533.
12. Glatz,E., Nilsson,R.P., Rutberg,L. and Rutberg,B. (1996) A dual role for the Bacillus subtilis glpD leader and the GlpP protein in the regulated expression of glpD: antitermination and control of mRNA stability. *Mol. Microbiol.*, **19**, 319–328.
13. Court,D.L., Gan,J., Liang,Y.H., Shaw,G.X., Tropea,J.E., Costantino,N., Waugh,D.S. and Ji,X. (2013) RNase III: genetics and function; structure and mechanism. *Annu. Rev. Genet.*, **47**, 405–431.
14. Nicholson,A.W. (2014) Ribonuclease III mechanisms of double-stranded RNA cleavage. *Wiley Interdiscip. Rev. RNA*, **5**, 31–48.
15. Herskovitz,M.A. and Bechhofer,D.H. (2000) Endoribonuclease RNase III is essential in Bacillus subtilis. *Mol. Microbiol.*, **38**, 1027–1033.
16. Oguro,A., Kakeshita,H., Nakamura,K., Yamane,K., Wang,W. and Bechhofer,D.H. (1998) Bacillus subtilis RNase III cleaves both 5′- and 3′-sites of the small cytoplasmic RNA precursor. *J. Biol. Chem.*, **273**, 19542–19547.

17. Mathy,N., Benard,L., Pellegrini,O., Daou,R., Wen,T. and Condon,C. (2007) 5′-to-3′ exoribonuclease activity in bacteria: role of RNase J1 in rRNA maturation and 5′ stability of mRNA. *Cell*, **129**, 681–692.
18. Redko,Y., Bechhofer,D.H. and Condon,C. (2008) Mini-III, an unusual member of the RNase III family of enzymes, catalyses 23S ribosomal RNA maturation in B. subtilis. *Mol. Microbiol.*, **68**, 1096–1106.
19. Panganiban,A.T. and Whiteley,H.R. (1983) Bacillus subtilis RNAase III cleavage sites in phage SP82 early mRNA. *Cell*, **33**, 907–913.
20. Mitra,S. and Bechhofer,D.H. (1994) Substrate specificity of an RNase III-like activity from Bacillus subtilis. *J. Biol. Chem.*, **269**, 31450–31456.
21. Durand,S., Gilet,L. and Condon,C. (2012) The essential function of B. subtilis RNase III is to silence foreign toxin genes. *PLoS Genet.*, **8**, e1003181.
22. Bardwell,J.C., Regnier,P., Chen,S.M., Nakamura,Y., Grunberg-Manago,M. and Court,D.L. (1989) Autoregulation of RNase III operon by mRNA processing. *EMBO J.*, **8**, 3401–3407.
23. Matsunaga,J., Dyer,M., Simons,E.L. and Simons,R.W. (1996) Expression and regulation of the rnc and pdxJ operons of Escherichia coli. *Mol. Microbiol.*, **22**, 977–989.
24. Lioliou,E., Sharma,C.M., Caldelari,I., Helfer,A.C., Fechter,P., Vandenesch,F., Vogel,J. and Romby,P. (2012) Global regulatory functions of the Staphylococcus aureus endoribonuclease III in gene expression. *PLoS Genet.*, **8**, e1002782.
25. Regnier,P. and Portier,C. (1986) Initiation, attenuation and RNase III processing of transcripts from the Escherichia coli operon encoding ribosomal protein S15 and polynucleotide phosphorylase. *J. Mol. Biol.*, **187**, 23–32.
26. Robert-Le Meur,M. and Portier,C. (1992) E.coli polynucleotide phosphorylase expression is autoregulated through an RNase III-dependent mechanism. *EMBO J.*, **11**, 2633–2641.
27. Stead,M.B., Marshburn,S., Mohanty,B.K., Mitra,J., Castillo,L.P., Ray,D., van Bakel,H., Hughes,T.R. and Kushner,S.R. (2011) Analysis of Escherichia coli RNase E and RNase III activity in vivo using tiling microarrays. *Nucleic Acids Res.*, **39**, 3188–3203.
28. Lybecker,M., Zimmermann,B., Bilusic,I., Tukhtubaeva,N. and Schroeder,R. (2014) The double-stranded transcriptome of Escherichia coli. *Proc. Natl. Acad. Sci. U.S.A.*, **111**, 3134–3139.
29. Gatewood,M.L., Bralley,P., Weil,M.R. and Jones,G.H. (2012) RNA-Seq and RNA immunoprecipitation analyses of the transcriptome of Streptomyces coelicolor identify substrates for RNase III. *J. Bacteriol.*, **194**, 2228–2237.
30. Lasa,I., Toledo-Arana,A., Dobin,A., Villanueva,M., de los Mozos,I.R., Vergara-Irigaray,M., Segura,V., Fagegaltier,D., Penades,J.R., Valle,J. *et al.* (2011) Genome-wide antisense transcription drives mRNA processing in bacteria. *Proc. Natl. Acad. Sci. U.S.A.*, **108**, 20172–20177.
31. German,M.A., Pillay,M., Jeong,D.H., Hetawal,A., Luo,S., Janardhanan,P., Kannan,V., Rymarquis,L.A., Nobuta,K., German,R. *et al.* (2008) Global identification of microRNA-target RNA pairs by parallel analysis of RNA ends. *Nat. Biotechnol.*, **26**, 941–946.
32. German,M.A., Luo,S., Schroth,G., Meyers,B.C. and Green,P.J. (2009) Construction of Parallel Analysis of RNA Ends (PARE) libraries for the study of cleaved miRNA targets and the RNA degradome. *Nat. Protoc.*, **4**, 356–362.
33. Addo-Quaye,C., Eshoo,T.W., Bartel,D.P. and Axtell,M.J. (2008) Endogenous siRNA and miRNA targets identified by sequencing of the Arabidopsis degradome. *Curr. Biol.*, **18**, 758–762.
34. Wang,W. and Bechhofer,D.H. (1997) Bacillus subtilis RNase III gene: cloning, function of the gene in Escherichia coli, and construction of Bacillus subtilis strains with altered rnc loci. *J. Bacteriol.*, **179**, 7379–7385.
35. Sharp,J.S. and Bechhofer,D.H. (2005) Effect of 5′-proximal elements on decay of a model mRNA in Bacillus subtilis. *Mol. Microbiol.*, **57**, 484–495.
36. Petit,M.A., Dervyn,E., Rose,M., Entian,K.D., McGovern,S., Ehrlich,S.D. and Bruand,C. (1998) PcrA is an essential DNA helicase of Bacillus subtilis fulfilling functions both in repair and rolling-circle replication. *Mol. Microbiol.*, **29**, 261–273.
37. Trevors,J.T. (1986) Plasmid curing in bacteria. *FEMS Microbiol. Rev.*, **32**, 149–157.
38. Deikus,G., Condon,C. and Bechhofer,D.H. (2008) Role of Bacillus subtilis RNase J1 Endonuclease and 5′-Exonuclease Activities in trp Leader RNA Turnover. *J. Biol. Chem.*, **283**, 17158–17167.
39. Sulthana,S. and Deutscher,M.P. (2013) Multiple exoribonucleases catalyze maturation of the 3′ terminus of 16S ribosomal RNA (rRNA). *J. Biol. Chem.*, **288**, 12574–12579.
40. Bechhofer,D.H., Oussenko,I.A., Deikus,G., Yao,S., Mathy,N. and Condon,C. (2008) Analysis of mRNA decay in Bacillus subtilis. *Methods Enzymol.*, **447**, 259–276.
41. Yao,S., Blaustein,J.B. and Bechhofer,D.H. (2007) Processing of Bacillus subtilis small cytoplasmic RNA: evidence for an additional endonuclease cleavage site. *Nucleic Acids Res.*, **35**, 4464–4473.
42. Gilet,L., DiChiara,J.M., Figaro,S., Bechhofer,D.H. and Condon,C. (2014) Small stable RNA maturation and turnover in Bacillus subtilis. *Mol. Microbiol.* , **95**, 270–282.
43. Nicolas,P., Mader,U., Dervyn,E., Rochat,T., Leduc,A., Pigeonneau,N., Bidnenko,E., Marchadier,E., Hoebeke,M., Aymerich,S. *et al.* (2012) Condition-dependent transcriptome reveals high-level regulatory architecture in Bacillus subtilis. *Science*, **335**, 1103–1106.
44. Markham,N.R. and Zuker,M. (2008) UNAFold: software for nucleic acid folding and hybridization. *Methods Mol. Biol.*, **453**, 3–31.
45. Belitsky,B.R. (2011) Indirect repression by Bacillus subtilis CodY via displacement of the activator of the proline utilization operon. *J. Mol. Biol.*, **413**, 321–336.
46. Huang,S.C., Lin,T.H. and Shaw,G.C. (2011) PrcR, a PucR-type transcriptional activator, is essential for proline utilization and mediates proline-responsive expression of the proline utilization operon putBCP in Bacillus subtilis. *Microbiology*, **157**, 3370–3377.
47. Moses,S., Sinner,T., Zaprasis,A., Stoveken,N., Hoffmann,T., Belitsky,B.R., Sonenshein,A.L. and Bremer,E. (2012) Proline utilization by Bacillus subtilis: uptake and catabolism. *J. Bacteriol.*, **194**, 745–758.
48. Dubnau,D. (1991) The regulation of genetic competence in Bacillus subtilis. *Mol. Microbiol.*, **5**, 11–18.
49. Hamoen,L.W., Eshuis,H., Jongbloed,J., Venema,G. and van Sinderen,D. (1995) A small gene, designated comS, located within the coding region of the fourth amino acid-activation domain of srfA, is required for competence development in Bacillus subtilis. *Mol. Microbiol.*, **15**, 55–63.
50. Turgay,K., Hahn,J., Burghoorn,J. and Dubnau,D. (1998) Competence in Bacillus subtilis is controlled by regulated proteolysis of a transcription factor. *EMBO J.*, **17**, 6730–6738.
51. Xu,W., Huang,J. and Cohen,S.N. (2008) Autoregulation of AbsB (RNase III) expression in Streptomyces coelicolor by endoribonucleolytic cleavage of absB operon transcripts. *J. Bacteriol.*, **190**, 5526–5530.
52. Li,H. and Nicholson,A.W. (1996) Defining the enzyme binding domain of a ribonuclease III processing signal. Ethylation interference and hydroxyl radical footprinting using catalytically inactive RNase III mutants. *EMBO J.*, **15**, 1421–1433.
53. Krasny,L. and Gourse,R.L. (2004) An alternative strategy for bacterial ribosome synthesis: Bacillus subtilis rRNA transcription regulation. *EMBO J.*, **23**, 4473–4483.
54. Pellegrini,O., Li de la Sierra-Gallay,I., Piton,J., Gilet,L. and Condon,C. (2012) Activation of tRNA maturation by downstream uracil residues in B. subtilis. *Structure*, **20**, 1769–1777.
55. Condon,C., Brechemier-Baey,D., Beltchev,B., Grunberg-Manago,M. and Putzer,H. (2001) Identification of the gene encoding the 5S ribosomal RNA maturase in Bacillus subtilis: mature 5S rRNA is dispensable for ribosome function. *RNA*, **7**, 242–253.
56. Daou-Chabo,R., Mathy,N., Benard,L. and Condon,C. (2009) Ribosomes initiating translation of the hbs mRNA protect it from 5′-to-3′ exoribonucleolytic degradation by RNase J1. *Mol. Microbiol.*, **71**, 1538–1550.
57. Sim,S.H., Yeom,J.H., Shin,C., Song,W.S., Shin,E., Kim,H.M., Cha,C.J., Han,S.H., Ha,N.C., Kim,S.W. *et al.* (2010) Escherichia coli ribonuclease III activity is downregulated by osmotic stress: consequences for the degradation of bdm mRNA in biofilm formation. *Mol. Microbiol.*, **75**, 413–425.
58. Regnier,P. and Hajnsdorf,E. (2009) Poly(A)-assisted RNA decay and modulators of RNA stability. *Prog. Mol. Biol. Transl. Sci.*, **85**, 137–185.

59. Sarkar,N. (1997) Polyadenylation of mRNA in prokaryotes. *Annu. Rev. Biochem.*, **66**, 173–197.
60. Campos-Guillen,J., Bralley,P., Jones,G.H., Bechhofer,D.H. and Olmedo-Alvarez,G. (2005) Addition of poly(A) and heteropolymeric 3′ ends in Bacillus subtilis wild-type and polynucleotide phosphorylase-deficient strains. *J. Bacteriol.*, **187**, 4698–4706.
61. Deutscher,M.P. (2009) Maturation and degradation of ribosomal RNA in bacteria. *Prog. Mol. Biol. Transl. Sci.*, **85**, 369–391.
62. Purusharth,R.I., Madhuri,B. and Ray,M.K. (2007) Exoribonuclease R in Pseudomonas syringae is essential for growth at low temperature and plays a novel role in the 3′ end processing of 16 and 5 S ribosomal RNA. *J. Biol. Chem.*, **282**, 16267–16277.
63. Davies,B.W., Kohrer,C., Jacob,A.I., Simmons,L.A., Zhu,J., Aleman,L.M., Rajbhandary,U.L. and Walker,G.C. (2010) Role of Escherichia coli YbeY, a highly conserved protein, in rRNA processing. *Mol. Microbiol.*, **78**, 506–518.
64. Jacob,A.I., Kohrer,C., Davies,B.W., RajBhandary,U.L. and Walker,G.C. (2013) Conserved bacterial RNase YbeY plays key roles in 70S ribosome quality control and 16S rRNA maturation. *Mol. Cell*, **49**, 427–438.
65. Britton,R.A., Wen,T., Schaefer,L., Pellegrini,O., Uicker,W.C., Mathy,N., Tobin,C., Daou,R., Szyk,J. and Condon,C. (2007) Maturation of the 5′ end of Bacillus subtilis 16S rRNA by the essential ribonuclease YkqC/RNase J1. *Mol. Microbiol.*, **63**, 127–138.
66. Brosius,J. (1992) Compilation of superlinker vectors. *Methods Enzymol.*, **216**, 469–483.
67. Ochi,K., Kim,J.Y., Tanaka,Y., Wang,G., Masuda,K., Nanamiya,H., Okamoto,S., Tokuyama,S., Adachi,Y. and Kawamura,F. (2009) Inactivation of KsgA, a 16S rRNA methyltransferase, causes vigorous emergence of mutants with high-level kasugamycin resistance. *Antimicrob. Agents Chemother.*, **53**, 193–201.